Europa's small impactor flux and seismic detection predictions

Daisuke Tsuji[a], Nicholas A. Teanby[b,*]

[a] *Department of Earth and Environmental Sciences, Nagoya University, Furocho, Chikusa, Nagoya 464-8601, Japan*
[b] *School of Earth Sciences, University of Bristol, Wills Memorial Building, Queens Road, Bristol, BS8 1RJ, UK*

Abstract

Europa is an attractive target for future lander missions due to its dynamic surface and potentially habitable sub-surface environment. Seismology has the potential to provide powerful new constraints on the internal structure using natural sources such as faults or meteorite impacts. Here we predict how many meteorite impacts are likely to be detected using a single seismic station on Europa to inform future mission planning efforts. To this end, we derive: (1) the current small impactor flux on Europa from Jupiter impact rate observations and models; (2) a crater diameter *versus* impactor energy scaling relation for icy moons by merging previous experiments and simulations; and (3) scaling relations for seismic signal amplitudes as a function of distance from the impact site for a given crater size, based on analogue explosive data obtained on Earth's ice sheets. Finally, seismic amplitudes are compared to predicted noise levels and seismometer performance to deter-

*Corresponding author
Email addresses: `tsuji.daisuke@d.mbox.nagoya-u.ac.jp` (Daisuke Tsuji), `n.teanby@bristol.ac.uk` (Nicholas A. Teanby)

mine detection rates. We predict detection of 0.002–20 small local impacts per year based on P-waves travelling directly through the ice crust. Larger regional and global-scale impact events, detected through mantle-refracted waves, are predicted to be extremely rare (10^{-8}–1 detections per year), so are unlikely to be detected by a short duration mission. Estimated ranges include uncertainties from internal seismic attenuation, impactor flux, and seismic amplitude scaling. Internal attenuation is the most significant unknown and produces extreme uncertainties in the mantle-refracted P-wave amplitudes. Our nominal best-guess attenuation model predicts 0.002–5 local direct P detections and 6×10^{-6}–0.2 mantle-refracted detections per year. Given that a plausible Europa landed mission will only last around 30 days, we conclude that impacts should not be relied upon for a seismic exploration of Europa. For future seismic exploration, faulting due to stresses in the rigid outer ice shell is likely to be a much more viable mechanism for probing Europa's interior.

Keywords: Europa, cratering, impact processes, geophysics, interiors

1. Introduction

Europa, the second of Jupiter's Galilean satellites, has long been considered an attractive target for lander missions due to its active surface processes and potentially habitable interior (Pappalardo et al., 2013). So far, Europa has been investigated using remote sensing by Voyagers 1 and 2 (1979, flyby missions passing through the Jovian system), Cassini-Huygens (2000, *en route* to Saturn), New Horizons (2006, *en route* to Pluto), and the Galileo Jupiter orbiter (1995–2003). Results from these missions are reviewed in detail by Pappalardo et al. (2009). Following these spacecraft observations the existence of liquid water beneath an icy outer shell has been proposed (e.g., Cassen et al., 1979; Carr et al., 1998; Kivelson et al., 2000). The sub-surface ocean is predicted to be in direct contact with a rocky mantle, giving rise to conditions analogous to those on Earth's seafloor (Gowen et al., 2011). The possibility of chemical interaction across the rock-water boundary has led to active discussion of a habitable sub-surface environment (e.g., Reynolds et al., 1983; McCollom, 1999; Chyba, 2000; Chyba and Phillips, 2001, 2002).

Although previous missions have taught us much about Europa and the Jovian system, many exciting questions remain unanswered (Squyres, 2011), particularly regarding surface activity and internal structure. Recently, the Jupiter Icy Moon Explorer (JUICE) orbiter mission was selected for the L1 launch slot of ESA's Cosmic Vision science programme to explore Jupiter and its potentially habitable icy moons including Europa (Grasset et al., 2013). Future missions could include a lander and one of the aims of NASA's recently announced Europa Clipper mission is to perform reconnaissance for future landing sites (Pappalardo et al., 2015). Some of the most recent mission configurations even include a lander element, with the potential to deliver instruments to the surface.

One of the best ways to probe icy moon interiors in any future mission will be with a surface-based seismic investigation. The Apollo seismic experiment, installed by astronauts, enhanced our knowledge of the lunar interior dramatically, including: lunar density (Bills and Ferrari, 1977), velocity structure (Goins et al., 1981; Nakamura, 1983; Lognonne et al., 2003), and seismic attenuation (Nakamura, 1976; Goins et al., 1981; Nakamura and

Koyama, 1982). On Mars, the Viking seismometer was intended to measure martian seismicity, but its position on the lander deck meant it was unable to capture any definitive seismic events due to poor coupling with the ground and sensitivity to wind noise (Anderson et al., 1976). NASA's 2018 InSight Mars lander aims to obtain more representative seismic data and will use a robot arm to deploy dual seismometers directly onto Mars' surface protected by a wind and thermal shield (Banerdt et al., 2013). On Europa, future missions may be able to deploy compact seismometers (e.g. Pike et al., 2010) to the surface in a cost effective way using penetrator technology (Collinson and UK Penetrator Consortium, 2008; Gowen et al., 2011).

Europa has a relatively small number of impact craters (Zahnle et al., 2003), which suggests a young and geologically active surface (Pappalardo et al., 2009). This makes it a promising target for seismic investigation as natural sources could be used to probe the internal structure (Lee et al., 2003; Panning et al., 2006). To aid future mission design it is important to predict in advance which kind of sources will produce the most detectable seismic signals. Two of the most promising seismic source candidates are: (1) fracturing or cracking of the ice crust driven by tidal forces; and (2) surface impacts by small comet- or asteroid-derived meteorites.

Fracturing of Europa's ice crust driven by tidally induced stresses is expected to be the main source of seismicity (Lee et al., 2003; Panning et al., 2006) and has been the main focus of research to date. The types and likely seismic magnitudes of such faulting are reviewed in detail by Panning et al. (2006) and include tensile cracks, normal faults, and strike-slip faults. The most common fracturing events are expected to be tensile cracking of the rigid outer ice shell driven by diurnal stresses induced by Europa's eccentric orbit around Jupiter. Estimates of diurnal stress range from 40–100 kPa (Hoppa et al., 1999; Leith and McKinnon, 1996) and should result in many small seismic events during each orbit, with crack depths of a few hundred metres and moment magnitudes of $M_w \sim 2$ (Lee et al., 2003; Panning et al., 2006). Note that moment magnitude M_w is commonly used to describe the size of an earthquake or planet-quake and is defined from the seismic moment M released in Nm according to $M_w = 2/3(\log_{10} M - 9.1)$ (Kanamori, 1977). Larger stresses of ~3-10 MPa can build up over longer time periods due to various mechanisms including Europa's asynchronous orbit, obliquity, polar wander, or ice shell freezing (McEwen, 1986; Wahr et al., 2009; Rhoden et al., 2011). These could result in much larger faulting events, such as the normal faults observed by Nimmo and Schenk (2006) that were estimated to require a driving stress of around 6–8 MPa and produce Europa-quakes with moment magnitudes of M_w ~5–6. Large strike-slip faults (McEwen, 1986) could result in similar sized events (Panning et al., 2006).

Large normal or strike-slip faults with M_w ~5 should be detectable globally at long-period with a reasonably high performance surface seismometer deployment, whereas much smaller events from diurnal tensile cracking would only be detectable locally (Panning et al., 2006). However, the exact occurrence rate of such seismic events includes extreme uncertainties as it depends on fracture/crack depth, crustal thickness, and the crust's depth-temperature profile, which are difficult to determine from current data. In addition, under the most plausible mission scenarios, which include only a single seismometer, it will be challenging to obtain the location and source mechanism details of a complex fault source. This will increase the uncertainty in any determinations of internal structure.

In contrast, meteorite impacts generate seismic energy during crater formation with a relatively simple isotropic source function (Teanby and Wookey, 2011), and could potentially be located using other methods such as surface imaging from an orbiting spacecraft (Malin et al., 2006; Daubar et al., 2013). The frequency of meteorite sources are also somewhat more predictable than that of fault sources and can be constrained by recent observations of impacts into Jupiter (Hueso et al., 2013) and crater populations on the Galilean satellites (Zahnle et al., 1998; Zahnle et al., 2003). In addition, future missions such as JUICE will improve our understanding of the small impactor population with high resolution imaging of Europa and Ganymede of up to 6 m/pixel (Grasset et al., 2013). Small locally detectable impacts would allow determination of the ice crust structure, whereas larger impacts could release enough energy to be detectable at teleseismic (global-scale) distances, which would be well suited to determining deep internal structure.

In this paper, we estimate how many impacts could be detected using a single surface-deployed seismometer, and determine whether impacts could provide a reliable additional source for a future seismic investigation of Europa.

2. Impacts on Europa

2.1. Current impactor flux

According to high-resolution images from the Galileo spacecraft, small impact craters are abundant on Europa (Bierhaus et al., 2001). However, the rate of small impacts that produce craters with diameters less than 1 km is poorly constrained by direct surface observations as a large number of small craters on Europa are "secondaries"; i.e. craters formed by material ejected from large primary impact craters (Bierhaus et al., 2005; Zahnle et al., 2008). Fortunately, the current small impactor flux into Jupiter is relatively well constrained by observations of impact flashes (Hueso et al., 2013). Therefore, to avoid the issues of secondary craters, our approach is to use Jupiter's impact flux observations, combined with the relative impact probability on Europa compared to Jupiter, to determine Europa's current impact rate.

Hueso et al. (2013) report the impact rate of small objects into Jupiter's atmosphere based on regular amateur astronomer observations of impact flashes, which provide a direct estimate of impact energy. In total three flashes were observed at times close to Jupiter's opposition, when many amateurs were able to observe the planet: one on June 3, 2010, one on August 20, 2010, and one on September 10, 2012. Hueso et al. (2013) used the measured light curves to estimate impactor energies and determine equivalent impactor diameters in the 5–20 m range by assuming a typical impact velocity of 60 $\mathrm{km\,s^{-1}}$ and densities in the range 250–2000 $\mathrm{kg\,m^{-3}}$. Hueso et al. (2013) then compare the impactor diameters with impactor diameter distributions estimated from crater counts (Zahnle et al., 2003; Schenk et al., 2004) and dynamical modelling (Levison et al., 2000). Based on estimates of the effective observation time coverage, Hueso et al. (2013) propose that around 12–60 objects with diameters of 5–20 m impact Jupiter each year and conclude that the impact rate of ecliptic comets estimated by Levison et al.

(2000) is the most consistent with their observations.

In the Jovian system, ecliptic comets (e.g. Jupiter-family comets) are generally regarded as the dominant source of primary craters (Zahnle et al., 1998; Zahnle et al., 2003; Burger et al., 2010). Asteroids from the main belt, Trojan, or Hilda groups provide a potential secondary impactor population. For example, Sánchez-Lavega et al. (2010) used orbital analysis to determine that the 2009 Jupiter impact event had a roughly equal probability of being an asteroid or comet. Subsequent near infrared observations of the impact site by Orton et al. (2011) indicated silicate spectral features, which favour an asteroidal origin for this impact. Conversely, the 1994 Shoemaker-Levy 9 impact displayed no such signature and a cometary origin is favoured for this impact (Orton et al., 2011). Burger et al. (2010) review the recent literature and conclude that the main belt asteroid contribution is likely to be negligible. However, modelling by Brunini et al. (2003) suggests that the Hilda group may provide a significant additional contribution to small crater production in the Jupiter system - perhaps comparable to the Jupiter-family comets - although this depends strongly on what is assumed about the unobserved small asteroid population and collision processes. Brunini et al. (2003) also suggest that impacts from the Trojans are approximately an order of magnitude less frequent than the Hildas. Furthermore, Di Sisto et al. (2005) find that asteroids escaped from the Hilda group can often mimic Jupiter-family comet orbits and so may be indistinguishable when it comes to cratering events. On balance it appears that while asteroids do impact Jupiter and its moons, their contribution is around an order of magnitude less than that from Jupiter-family comets.

In any case, independent of the source of the material, the model of Levison et al. (2000) provides the best agreement with the most direct observations of present-day impactor diameters available (Hueso et al., 2013). Zahnle et al. (2003) show Europa's ecliptic comet impact probability relative to Jupiter, $P_{\mathrm{EC}} = 6.6 \times 10^{-5}$, by using the Monte Carlo algorithm described by Zahnle et al. (1998, 2001). Using this scale factor, we rescale the Levison et al. (2000) model to compute the impactor diameter distribution on Europa, which is shown in Fig. 1 along with previous observational and model estimates. We employ a factor of two estimated uncertainty on this rate following Sánchez-Lavega et al. (2010). Note that for a given impactor size, the impact energy will be different for Jupiter and Europa as they have different typical impact velocities: $\sim$60 $\mathrm{km\,s^{-1}}$ for Jupiter and $\sim$26 $\mathrm{km\,s^{-1}}$ for Europa.

2.2. Crater diameter - impactor energy relation in Ice

We now consider the relation between impactor energy and crater diameter for icy surfaces. This allows both impactor and cratering rates for Europa to be considered and will later allow cratering events to be compared with analogue explosive experiments on ice sheets. The relation between an impactor's kinetic energy E and the resulting crater diameter D is usually expressed as a simple power-law form: $D = \alpha E^{\beta}$, where α and β are positive constants. The exponent β theoretically takes different values between 1/3 and 1/4 depending on the regime of the cratering conditions, which can be derived by a simple scaling approach (Katsuragi, 2015). The small craters considered here are in the strength regime (Melosh, 1980, 1989). The exponent β is also influenced by effects such as target/impactor material properties and impact angle (Holsapple and Schmidt, 1982; Horedt and Neukum, 1984). To avoid such complexity, a single scaling law for the $D - E$ relation is used for this study, and variations in target and impact conditions are included as an extra uncertainty term.

We used the cratering database (CDB) of Holsapple (2015) to determine the scaling law for ice, which includes high energy impact studies and explosive experiments. Compared to the number of CDB measurements for rocky surfaces, the data for icy surfaces is rather sparse due to the more complex experimental setups required. To cover a wider range of impact energy, and obtain enough data to determine an accurate scaling law, we also include additional ice experimental data (Lange and Ahrens, 1987; Iijima et al., 1995) and impact crater simulations (Turtle and Pierazzo, 2001; Bray, 2009; Bray et al., 2014).

Lower gravity in general makes craters easier to excavate and the gravity on Europa is 1.31 ms^{-2} compared to 9.81 ms^{-2} on Earth. Horedt and Neukum (1984) present a compilation of crater-related scaling laws, which are applicable to different gravity conditions. For impacts into icy bodies, the gravity affects crater diameters by a factor of $(g_\oplus/g)^{0.25}$, where g and $g_\oplus$ are the surface gravity on the planet and on Earth respectively. Kawakami et al. (1983) have previously applied this gravity scaling to craters on Mimas (Saturnian satellite) and Callisto (Jovian satellite). Therefore, the general scaling law for crater diameter as a function of impactor energy, including the gravity effect, is of the form:

$$D = \alpha_\oplus E^\beta \left(\frac{g_\oplus}{g}\right)^{0.25} = \alpha E^\beta, \tag{1}$$

where $\alpha = \alpha_\oplus (g_\oplus/g)^{0.25}$ relates experimental results obtained on Earth to a general planet.

Figure 2 shows energy versus crater diameter for our overall ice database under Earth gravity conditions. Because the simulations of Turtle and Pierazzo (2001), Bray (2009), and Bray et al. (2014) were carried out under Europa and Ganymede gravity conditions respectively, the results were rescaled to Earth gravity first by applying the above gravity scaling, which allows all the data to be compared on the same plot. Although the data are quite sparse, most of the data lie on a single line on a double logarithmic plot. The parameters $\alpha_{\oplus}$ and β were fitted using least squares. Our overall scaling law for general icy bodies including uncertainties for unknown source/target parameters and a gravity correction is given in SI units by:

$$D = 1.82^{+0.85}_{-0.57} \times 10^{-2} E^{0.29\pm0.002} \times \left(\frac{g_{\oplus}}{g}\right)^{0.25}. \quad (2)$$

Note that error bars on the constant of proportionality are chosen so that the resulting uncertainty range encompasses 68% of the measured data, while those on the power are formal 1σ errors from the least-squares fitting method. Therefore, these error bars are representative of a single cratering event with unknown impactor density and incidence angle. Figure 2 also shows the scaling relation for rocky surfaces derived by Teanby and Wookey (2011) for comparison, which is not so different from that for icy surfaces in this diameter range. The main difference between impacts in ice and rock is that β is slightly larger for rock than for ice, meaning that small craters are easier to form in ice. This agrees with laboratory studies, which show craters in ice are about 2–3 times larger than in rock for experiments at low impact energies $E < 1$ KJ (Lange and Ahrens, 1987).

Previously, Zahnle et al. (2003) proposed a more complex scaling relation:

$$D = 11.9 \times 10^3 \left(\frac{v^2 \times 10^{-6}}{g \times 10^2} \right)^{0.217} \left(\frac{\rho_\mathrm{i}}{\rho_\mathrm{t}} \right)^{0.333} (d \times 10^{-3})^{0.783}, \tag{3}$$

where the d is the impactor diameter (all parameters are given in SI units), which was based on scaling relations derived for small impacts and explosions in sand by Schmidt and Housen (1987). Zahnle et al. (2003) assume an impact velocity $v = 2.6 \times 10^4$ ms^{-1}, Europa's surface gravity $g = 1.31$ ms^{-2}, an impactor density ρ_i=600 kg m^{-3}, and a target density ρ_t=900 kg m^{-3}. Under these assumptions and Earth's gravity, their relation simplifies to:

$$D = 5.69 \times 10^{-2} E^{0.261} \tag{4}$$

We plot this against our scaling relation in Fig. 2 as an additional check. The resulting predictions are within our calculated scaling law uncertainties for crater diameters over 100m. However, for smaller craters the Zahnle et al. (2003) relation predicts crater diameters up to three times larger than our scaling law. This is due to the fact that at low energies craters are much easier to form in sand than in ice so the Zahnle et al. (2003) relation becomes less applicable. We consider our compilation of ice impacts more appropriate for the present study and so use our simplified scaling relation (Eq. 2) for the rest of this paper. This has the additional advantage of not requiring assumptions about impactor densities. Instead, using Eq. 2 enables us to convert directly between impact energy and a corresponding crater diameter on Europa, including an uncertainty, which is more useful for the analysis in this study.

3. Seismic signals from impacts in ice

In this section we determine the amplitude of a seismic signal as a function of distance for a given crater forming impact. Explosions are commonly used as analogues for impact processes (Teanby and Wookey, 2011). Therefore, our approach is to use analog explosive data obtained on Earth's icy surfaces to empirically determine seismic signal amplitudes and associated uncertainties. The advantage of this approach compared to entirely theoretical waveform modelling is that we do not need to explicitly consider seismic efficiency, the fraction of impact energy converted into seismic waves, which is extremely uncertain (Richardson et al., 2005; Teanby and Wookey, 2011). Both impacts and explosives are high frequency sources, meaning that the bulk of the near-field seismic energy will be in high frequency waves, which are quickly attenuated in an attenuating medium like ice. Therefore, accurate seismic efficiency determination would require extremely high frequency seismic measurements to be taken at multiple locations close to the source, which are typically not obtained. Using analogue data avoids the need for such measurements and intrinsically accounts for near-field and source effects. However, scaling relations base on terrestrial ice sheet data must be modified before they can be applied to Europa.

For our case of impact induced seismicity we focus on first arrival P-waves (primary or compressional waves) rather than S-waves (secondary or shear waves) because the most energetic phases for non-shear sources like impacts are P-waves (Teanby and Wookey, 2011). Therefore, S-wave amplitudes are not considered in this study. In addition, we suppose the seismometer established on Europa is a velocity sensor and measures the ground velocity induced by seismic waves. Here the peak signal amplitude (i.e., the maximum ground velocity) of the first arrival wave is regarded as a representative distinct amplitude.

3.1. Terrestrial distance-energy-amplitude relation for ice covered rock

First arriving P-waves in terrestrial ice sheets are either direct ice waves, which only propagate through the ice, or refracted phases, which are refracted at the ice-rock interface. For typical ice velocities (4 $\mathrm{km\,s^{-1}}$) and rock velocities (6–8 $\mathrm{km\,s^{-1}}$) with an ice sheet thickness of 2–4 km, the direct ice wave arrives first for source-receiver distances of <5–10 km and the refracted wave arrives first for distances >5–10 km. We note that the refracted wave provides a reasonable analogue to Europa, with suitable corrections for the presence of an ocean and differences in layer thicknesses. However, the direct P-wave in terrestrial ice sheets is a poor analogue for offsets (source-receiver distances) much greater than 10 km as an ice layer bounded at the bottom by high velocity rock acts as a wave guide for moderate to high incidence angle waves, which maintains a relatively high amplitude (see e.g. Shulgin and Thybo, 2015). This will not be the case on Europa where the low velocity ocean layer refracts waves impinging on the ice bottom boundary downwards, where they are either refracted into the mantle (low incidence angles) or trapped in the low velocity ocean layer (moderate to high incidence angles).

3.1.1. Analogue dataset 1: East Antarctica

Explosive experiments on ice were carried out in East Antarctica by the Japanese Antarctic Research Expedition in 1979–1981 (Ikami et al., 1981;

Ito and Ikami, 1984). In these studies, 5 small shots were fired in shallow drill holes (depth: $\leq$ 64 m, explosive size: $\leq$ 560 kg TNT) along with a couple of large explosions in deeper drill holes (depth: $\geq$ 64m, explosive size: $\geq$ 1000 kg TNT). Several seismometers were deployed on the ice and seismic amplitudes were measured as a function of source-receiver offset. Because the thickness of ice on East Antarctica is a few kilometres, which is within an order of magnitude of the predicted thickness of Europa's crust (Carr et al., 1998; Greenberg et al., 1998, 1999; Turtle and Pierazzo, 2001; Nimmo et al., 2003; Moore, 2006; Bray et al., 2014), these explosive experiments can, with suitable adjustment, be used as an impact analogue for Europa.

The analogue ice data imply that the seismic efficiency of large shots is higher than that of small shots. This is most likely due to the ice density at the explosion locations; shot points for the shallow small explosions are covered with very porous ice (i.e., snow or firn) in contrast to more solid ice (density: 850–900 $\mathrm{kg\,m^{-3}}$) for the deeper holes of the large shots. In other words, the denser the ice at the point of explosion, the higher the seismic efficiency. Europa's surface is unlikely to be snow-like or have a significant thickness of highly gardened material, otherwise the detailed tectonic features and cracking would be difficult to see (e.g., Greeley et al., 2000; Greeley et al., 2004). Therefore, we assume Europa has a more competent solid ice surface, which implies shots in solid ice will be better analogues of impact processes on Europa.

The overall frequency response of the seismometers used was flat from 2 to 20 Hz, which was sufficient to observe the most energetic P-wave arrivals, which had frequencies in the range 5–15 Hz (Ito and Ikami, 1984).

Interestingly, Ito and Ikami (1984) also report that the amplitudes generated in deep solid ice show a similar dependence on the source-receiver distance to explosive experiments in rock. No distinction was given between direct and refracted waves in this study. However, given offsets in this experiment ranged from 0.5–200 km the amplitudes reported represent those of both the direct ice wave (distances $\lesssim$10 km) and the crustal refracted wave (distances $\gtrsim$10 km).

3.1.2. Analogue dataset 2: East-central Greenland

Shulgin and Thybo (2015) report results from more recent explosive experiments in East-central Greenland. They fired 8 shots in total, whose explosive charge sizes were in the range 500–1000 kg in deep boreholes with depths of about 80 m. The thickness of the ice sheet in East-central Greenland is 2–3.5 km, also within an order of magnitude of Europa's estimated ice crust thickness. For source-receiver distances of 10 km or less the direct P-wave (passing though the ice only) was the first arrival, whereas at greater distances the crustal refracted wave was the first arrival. Shulgin and Thybo (2015) report the dependence on source-receiver distance of the maximum amplitude of the direct ice wave, refracted crustal phases, and refracted mid-crustal phases/Moho reflections. The frequency of the direct ice wave covered a broad frequency band from $\sim$5–40 Hz at small offsets, while the refracted waves had peak frequency content of 5–15 Hz at large range ($>$100 km).

3.1.3. Terrestrial scaling relation - refracted P-wave

Seismogram amplitude for a general terrestrial ice sheet can now be estimated using the above explosion experiments. The amplitude data are shown as a function of source-receiver distance in Fig. 3. Data with offsets over 10 km are representative of the refracted P-wave. To allow data with different explosive yields to be shown on the same plot, measured ground velocities are normalised relative to a 1000 kg TNT reference shot by using the scaled velocity-amplitude:

$$A_{\text{scaled}} = A_{\text{measured}} \left(\frac{E_{\text{ref}}}{E} \right)^{c} \tag{5}$$

where A_{measured} is the peak amplitude of ground velocity measured from the seismogram, E_{ref} is the energy corresponding to 1000 kg TNT, E is the yield of the explosive used, and c is 0.5 (Teanby, 2015). Note that Ito and Ikami (1984) report peak-to-peak amplitudes of seismic waves so we use half of those values for the representative maximum amplitudes. Also, for the explosives in East-central Greenland, we only show the refracted wave data for shot point 1 of Shulgin and Thybo (2015) in Fig. 3 (extracted from their Figure 9) as this shot has physical amplitude units specified.

Fig. 3 also shows the impact and explosion data for rocky surfaces presented by Teanby (2015) for comparison, which cover ranges $\leq$1200 km. For unit conversions from kg TNT into Joules, we assume 1kg TNT $= 4.18 \times 10^{6}$J (Shoemaker, 1983). The linear trend in Fig. 3 suggests that for explosions recorded on terrestrial ice sheets the relation between the velocity-amplitude $A_{\oplus_{\text{explosion}}}$ and the source-receiver distance x can be empirically expressed as:

$$A_{\oplus_{\text{explosion}}} = A_{\text{ref}} \left(\frac{x}{x_{\text{ref}}} \right)^{b} \left(\frac{E}{E_{\text{ref}}} \right)^{c}, \tag{6}$$

where A_{ref} is the amplitude of a reference event with yield E_{ref} at distance x_{ref}, b is a power law exponent for distance which includes the effects of attenuation and geometrical spreading, and c is a power law exponent for the yield dependence. Parameter A_{ref} includes the effects of source coupling and seismic efficiency. Here we chose a reference event with a yield equivalent to 1000 kg TNT and a reference distance of 10 km. From energy conservation only, c should be 1/2 because the kinetic energy of an elastic wave is proportional to the ground velocity squared. However, values of c from 1/3–1 have been reported in the literature, as reviewed by Kohler and Fuis (1992). Here we follow Teanby (2015) and use $c = 1/2$, which also fits the ice data used here. Parameter b should be approximately -1 for spherically propagating waves in an isotropic medium without intrinsic/scattering attenuation (Shearer, 2009). However, in a general case the value of b tends to be less than -1. Note that parameter b can be assumed to be the same for both explosions and impacts because the effect of source-receiver distance entirely depends on crustal properties and wave propagation (Teanby, 2015).

The best fitting A_{ref} value has a different value for explosions and impacts, with explosions giving higher peak velocity-amplitudes than impacts (Teanby, 2015). This is primarily because explosives are buried to improve seismic coupling, whereas impacts occur at the surface. Therefore, when estimating the amplitude of meteorite impacts from explosive experiment data, a scaling factor s needs to be included in Eq. 6, which gives the velocity amplitude due to impacts $A_{\oplus_{\mathrm{impact}}}$ as:

$$A_{\oplus_{\mathrm{impact}}} = sA_{\mathrm{ref}} \left(\frac{x}{x_{\mathrm{ref}}}\right)^b \left(\frac{E}{E_{\mathrm{ref}}}\right)^c, \qquad (7)$$

where the value of s is $\approx$0.1 with a factor of four uncertainty (Teanby, 2015), implying that buried explosions are approximately 10 times more effective at generating seismic waves than impacts. For the rocky data presented by Teanby (2015), all raw data were bandpass filtered between 1 and 16

Hz, which covered the most energetic phases. Since this frequency range also corresponds to the most energetic phases of explosive data in ice, the amplitude data of Ikami et al. (1981) and Shulgin and Thybo (2015) can be directly compared with the rocky surface velocity-amplitudes.

For the explosions in East Antarctica, scaled velocity-amplitudes of large shots (1000 and 1400 kg TNT), which were fired in dense ice, lie within the error of the explosions scaling law for rocky surfaces (Fig. 3). This was also noted by Ito and Ikami (1984). Explosions in East-central Greenland were also conducted in deep holes, so as expected the data of Shulgin and Thybo (2015) overlap with that of Ito and Ikami (1984). In contrast, the data from small shots (10, 20, 45, 100, and 560 kg TNT) exploded in shallow/porous ice fall below the line of best fit for the large explosions, due to a reduced seismic efficiency. As noted earlier, we consider shots in solid ice as the best analogue for Europa's surface. The seismic data from small shots in Ito and Ikami (1984) are then not an appropriate analogue for Europa's surface conditions, so only the two largest shots (1000 and 1400 kg TNT) from this study are used here.

The ice data in Fig. 3 show that the explosions scaling law of Teanby (2015) - derived from nuclear explosives, chemical explosives, and impact events at ranges of 0–1200 km - can also be directly used for icy conditions as it fits the ice analogue datasets well.

Parameter values are summarised in Table 1. These parameters are representative for a refracted wave propagating through Earth's rocky or ice covered crust. The parameters are valid over the range of source data used, i.e. offsets $\leq$1200 km and the 1–16 Hz frequency range.

3.1.4. Terrestrial scaling relation - direct ice wave

The direct ice wave is a much simpler case and can be derived from a reference explosion in ice with amplitude A'_{ref}, energy E_{ref}, and distance x_{ref}. The direct P-wave distance trend reported by Shulgin and Thybo (2015) is not directly applicable to Europa because of the waveguide effect of the low velocity ice sheet. Therefore, we use the measured direct ice wave amplitude at 10 km distance. At this small offset the waveguide effect can be neglected and the amplitude is representative. Using a reference explosion the amplitude of the direct ice wave $A'_{\oplus_{\mathrm{impact}}}$ is thus given by:

$$A'_{\oplus_{\mathrm{impact}}} = sA'_{\mathrm{ref}} \left(\frac{x}{x_{\mathrm{ref}}}\right)^{-1} \left(\frac{E}{E_{\mathrm{ref}}}\right)^{c} \exp\left(-\frac{\pi f(x - x_{\mathrm{ref}})}{v_i Q_p}\right), \quad (8)$$

where the $(x/x_{\mathrm{ref}})^{-1}$ term accounts for spherical geometric spreading in an isotropic medium and the exponential term allows for intrinsic attenuation at frequency f for ice velocity v_i and P-wave quality factor Q_p. The seismic quality factor Q allows quantification of the energy lost due to anelastic processes, such as grain boundary friction, during propagation of seismic waves. If a seismic wave with energy e loses Δe per cycle then $Q = 2\pi e/\Delta e$ (Shearer, 2009). High Q materials have low attenuation and low Q materials have high attenuation. For a given medium, Q for compressive P-waves Q_p is generally higher than for S-waves Q_s, which generally suffer more intrinsic attenuation.

For x_{ref}=10 km and $E_{\mathrm{ref}} = 4.18 \times 10^9$ J (≡1000 kg TNT) measured amplitudes are between 10^{-5} ms^{-1} (Ito and Ikami, 1984) and 10^{-4} ms^{-1} (Shulgin and Thybo, 2015). Therefore, we use the geometric mean value of $A'_{\mathrm{ref}} = 3 \times 10^{-5}$ ms^{-1} with a factor of three uncertainty. Parameters s and c

are the same as for the refracted wave case as they relate to source processes only.

3.2. Seismic amplitude distance relations for Europa

We now consider application of our terrestrial ice sheet amplitude scaling relations to the specific case of Europa. First, we develop a reasonable set of seismic models for Europa's interior. Second, we determine which seismic phases are most important for our study. Finally, we use a simple ray tracing approach to determine correction factors to allow the terrestrial ice sheet amplitude scaling relations to be applied to Europa.

3.2.1. Europa interior structure

Observations of Europa's mass and moment of inertia support a four layer internal structure comprising a thin ice crust, a liquid ocean layer, a silicate mantle, and a dense iron core (Anderson et al., 1998; Kuskov and Kronrod, 2001, 2005; Sohl et al., 2002).

The ice crust is thought to comprise two distinct sub-layers: (1) a cold rigid (stagnant) lid with a steep temperature gradient, where internal heat is transferred by conduction, and (2) a warmer convecting deeper layer with an approximately isothermal or adiabatic temperature profile (Mitri and Showman, 2005; Moore, 2006). The total ice shell thickness is estimated to be $\sim$20 km (Nimmo et al., 2003; Moore, 2006), with a conductive lid thickness of $\sim$5 km (Nimmo and Manga, 2002; Nimmo et al., 2003). Thermal models estimate the convective layer temperature to be $\sim$250 K, around 20 K below the estimated ocean temperature of 270 K (Nimmo and Manga, 2002).

Cammarano et al. (2006) present a range of possible internal models for

Europa's deep structure assuming pyrolitic or chondritic mantles, pure iron or iron plus 20% sulphur core, and two end member temperature profiles. The composition, temperature, and size of the core and mantle cannot be uniquely constrained based on the available data. Despite this, for physically consistent models the seismic velocities and densities in the ice crust, ocean layer, and mantle are relatively similar for all models, as is the ocean layer depth (110–140 km) (Cammarano et al., 2006). However, mantle attenuation, core size and core seismic velocities and densities can take a wide range of values. Most importantly for this study are the extreme uncertainties in attenuation and seismic quality factor Q in the interior, originating from uncertainty in the internal temperature profile. End member models from Cammarano et al. (2006) have shear wave quality factor Q_s spanning values from 100 (highly attenuating) to above 10^7 (effectively no attenuation at seismic frequencies). This uncertainty will have a strong influence on the amplitude of seismic waves.

In this paper, we use a representative set of internal models with average seismic velocities, densities and layer boundaries based on the "cold" scenario from Cammarano et al. (2006). The choice of this model is not critical as seismic velocities are similar for both "cold" and "hot" cases. For simplicity we also assume a uniform velocity and density in each layer, which we consider reasonable as the pressure gradients in Europa's interior are relatively modest, leading to shallow gradients in layer properties. To account for the large uncertainty in Q we consider three attenuation models:

1. **Low** Q (high attenuation): Q_p=20 is assumed in the outer ice shell, which is similar to frozen water-NaCl mixtures with temperatures above

the eutectic, resulting in partial melting (i.e. water ice and brine pockets) (Spetzler and Anderson, 1968). Q_p=225 is assumed in the mantle based on a typical mid-mantle value from Cammarano et al. (2006)'s "hot" model. This is very much a worst-case scenario with the maximum possible attenuation that could be considered reasonable.

2. **Nominal** Q: Q_p=65 is assumed in the outer ice shell; similar to the Athabasca glacier (Canada), which is very close to its melting point (Clee et al., 1969). Q_p=1350 is assumed in the mantle based on the value for Earth's mid-crust (Dziewonski and Anderson, 1981), which falls between Cammarano et al. (2006)'s end member cases. We regard this case as a reasonable approximation to Europa's interior.

3. **High** Q (Low attenuation): Q_p=200 is assumed in the outer ice shell, which is similar to values in cold terrestrial ice sheets 20 K or more below their freezing point (Bentley and Kohnen, 1976; Peters et al., 2012). Q_p=2.25×10^4 is assumed in the mantle based on a typical mid-mantle value in Cammarano et al. (2006)'s "cold" model. This case has effectively no attenuation in the interior, very little attenuation in the outer ice shell, and in our view is extremely optimistic.

For non-liquid layers Q_s is assumed to be 4/9$^{\text{ths}}$ of Q_p, i.e. the value for a standard linear solid (Shearer, 2009). P-wave propagation in water is known to suffer very little attenuation (Sheehy and Halley, 1957) and attenuation in the ocean layer will have a negligible effect on seismic amplitudes. For all models the ocean layer is assumed to have Q_p=5000. This is the value for a 2 Hz seismic wave extrapolated from a least squares fit of explosion measurements in the Pacific (Vadov, 2006) to an attenuation power law derived by Sheehy and Halley (1957). For Europa's core we assume Q_p=190 in all models, a rather pessimistic value based on Earth's core (Dziewonski and Anderson, 1981). We could reasonably expect much higher Q_p for Europa's core because of the lower internal temperature. For example, Cammarano et al. (2006)'s cold model has Q_p=2.25×10^4. However, this assumption does not affect our analysis as we do not consider core phase amplitudes. Our simplified interior models are summarised in Table 2.

3.2.2. First arriving seismic phases

To inform the corrections required for applying the analogue ice sheet measurements to Europa, we use full waveform modelling to predict the first arriving and most energetic phases. Full-waveform synthetic seismograms were generated using the direct solution method (DSM) (Geller and Ohminato, 1994; Geller and Takeuchi, 1995; Takeuchi et al., 1996) with our nominal Q simple interior model. The DSM method was too computationally expensive to model a high frequency surface event, so as an approximation we chose to model an isotropic explosive source at 10 km depth to a maximum frequency of 0.5 Hz using a 4000 layer model with a maximum spherical harmonic degree of 4000. This was sufficient to determine the first arrival phases and approximate relative amplitudes to guide modifications to the scaling relations. Arrivals were identified using the Tau-p toolkit (Crotwell et al., 1999). Both the DSM and Tau-p codes are used extensively for terrestrial applications and only required a minor modification for planet radius for our application. Figure 4 shows the resulting seismic record section. We make a slight addition to the usual seismic phase nomenclature and use "M" to denote propagation though the mantle and "K" to denote propagation through the core (Europa has no known inner core). Hence, the direct ice wave is called "P", the refracted mantle phase is called "PMP" and the wave passing through the core is called "PMKMP".

Europa has a low velocity ocean layer underlying the ice crust and the modelling shows that this structure simplifies the first arriving phases into: the direct P-wave (passing though the ice) for offsets from 0–35°, the refracted mantle PMP-wave (passing though the ice, ocean, and mantle) for offsets from 35–140°, and the weak core diffracted PMP P-wave for offsets over 140° (although the core traversing PMKMP P-wave is expected to be much stronger). Note that as the core is relatively small its shadow zone only affects offsets over 140°, so our simple assumptions about its seismic properties will have limited effects on the results. Based on this modelling, the main phases we need to consider for impact detection are the direct P-wave through the ice crust and the PMP-wave which passes though the ice crust, ocean, and mantle. We do not consider core phases further in this paper.

3.2.3. Seismic ray tracing

The waveform modelling shows that direct P and refracted PMP are the most important phases for impact detection. Application of the amplitude scaling relations in Eqs. 7 and 8 to Europa will require calculation of correction factors, which depend on details of the path travelled by the waves. Therefore, we now develop a simple ray tracing approach to calculate path lengths and incidence angles as a function of source receiver offset. Figure 5 compares ray paths for the ice sheet data and Europa's interior.

First consider the terrestrial case. We approximate the terrestrial ice sheet data with a two layer planar model, as the curvature of the Earth can be neglected over the scales of the surveys. From the ice sheet data we know the amplitude for a given source-receiver distance x from Eq. 7, which comprises propagation distances of x_r in rock and $2x_i$ in ice (see Figure 5a). For a refracted wave, the angle of incidence θ at the ice-rock boundary will be close to the critical angle θ_c determined using Snell's law:

$$\sin\theta_c = \frac{v_i}{v_r} \tag{9}$$

For typical velocities θ_c =30–45°. Therefore, in terms of the ice layer thickness z we have:

$$x_r \approx x - 2z\tan\theta_c \tag{10}$$

For the ice sheet data $z = 2 - 3.5$ km, so at the large offsets of interest the $\tan\theta_c$ term can be neglected and $x \approx x_r$. Therefore, for refracted arrivals in terrestrial ice sheets the scaling relation in Eq. 7 can be considered a function of propagation distance through the rock only, coupled by a negligible layer of surface ice, i.e. $A_E(x) \approx A_E(x_r)$.

Now consider Europa's top three layers: layer 1 the ice crust; layer 2 the water ocean; and layer 3 the rocky mantle. We define $s_{1,2,3}$ as the single segment path lengths in each layer (Figure 5b); $r_{1,2,3}$ as the planet centre to layer top distances (note that r_1 is the planet radius); and $v_{1,2,3}$ as the P-wave velocities. Because the layer velocities are uniform in our simple model, ray paths can be calculated analytically using ray theory (Aki and Richards, 2002). The spherical ray parameter p is conserved along a ray path and is defined by $p = ru\sin\theta$, where at any given point along the ray path r is the distance to the planet centre, u is the slowness (1/velocity), and θ is the incidence angle (Shearer, 2009). Using the sine and cosine rules, the path lengths in each layer can be shown to be:

$$s_1^2(p) = r_1^2 + r_2^2 - 2r_1r_2\cos\left(\sin^{-1}\frac{pv_1}{r_2} - \sin^{-1}\frac{pv_1}{r_1}\right) \quad (11)$$

$$s_2^2(p) = r_2^2 + r_3^2 - 2r_2r_3\cos\left(\sin^{-1}\frac{pv_2}{r_3} - \sin^{-1}\frac{pv_2}{r_2}\right) \quad (12)$$

$$s_3^2(p) = 2r_3^2\left(1 - \cos\left(\pi - 2\sin^{-1}\frac{pv_3}{r_3}\right)\right) \quad (13)$$

with an overall source-receiver offset angle of:

$$\Delta(p) = 2\left(\sin^{-1}\frac{pv_1}{r_2} - \sin^{-1}\frac{pv_1}{r_1} + \sin^{-1}\frac{pv_2}{r_3} - \sin^{-1}\frac{pv_2}{r_2} - \sin^{-1}\frac{pv_3}{r_3} + \pi\right) \quad (14)$$

Equations 11–14 can be used to tabulate the angular offset Δ (or the linear offset $x = r_1\Delta$) and the path lengths $s_{1,2,3}$ as a function of p for our simple interior models. The angle of incidence at each boundary can be trivially determined from the ray parameter $p = ru\sin\theta$ at each interface encountered by the ray. Figure 6(a–e) shows p, travel time, and $s_{1,2,3}$ as a function of Δ for the PMP-wave.

3.2.4. Europa direct P-wave

For the direct ice P-wave, the amplitude scaling relation (Eq. 8) can be used directly, with a slight modification for differences in Q between Europa's crust and terrestrial ice sheets.

$$A'_{E_{\mathrm{impact}}} = sA'_{\mathrm{ref}}\left(\frac{x}{x_{\mathrm{ref}}}\right)^{-1}\left(\frac{E}{E_{\mathrm{ref}}}\right)^{c}\exp\left(-\frac{\pi f x}{v_1Q_1}\right)\exp\left(+\frac{\pi f x_{\mathrm{ref}}}{v_iQ_{1\oplus}}\right), \quad (15)$$

where $Q_{1\oplus}$ is the P-wave Q in terrestrial ice sheets, assumed to be $Q_{1\oplus}$=65 (Clee et al., 1969) and v_i is the P-wave velocity in ice, which can be assumed to be the same on Europa and Earth (v_i=v_1=4 km s^{-1}). The 4 km s^{-1} P-wave velocity in ice is consistent with the direct ice wave observed by Shulgin and Thybo (2015) in the Greenland ice sheet.

3.2.5. Europa mantle-refracted P-wave

For the mantle-refracted PMP-wave, the amplitude scaling relation (Eq. 7) requires significant modification to account for differences in structure and geometry between the analogue ice sheets and Europa's interior. The three main differences are: (1) Increased geometrical spreading due to differences in path lengths in the ice, water, and rock layers; (2) Differences in transmission coefficients due to the additional water ocean layer on Europa; and (3) Attenuation in Europa's ice crust, water ocean, and rocky mantle.

Therefore, when applied to Europa the most relevant length is the propagation distance through Europa's rocky mantle s_3.

The corrected version of Eq. 7 for mantle-refracted waves then becomes:

$$A_{E_{\text{impact}}} = sA_{\text{ref}} \left(\frac{s_3}{x_{\text{ref}}} \right)^b \left(\frac{E}{E_{\text{ref}}} \right)^c f_{\text{trans}} f_{\text{geom}} f_{\text{atten}}, \tag{16}$$

where f_{trans}, f_{geom} and f_{atten} are correction factors for transmission coefficients, geometrical spreading, and attenuation respectively. Note that s_3 is analogous to x_r ($\approx x$) in the terrestrial ice sheet data.

Correction for geometrical spreading: The path length though the rocky mantle s_3 is analogous to x_r in the ice sheet data, so geometric spreading in the mantle is already accounted for in Eq. 7. However, we must also include extra geometric spreading due to the additional ice and ocean paths. As the layers have a uniform velocity we can assume spherical wave propagation (amplitude proportional to 1/distance). Therefore, the amplitude correction factor for geometric spreading is:

$$f_{\text{geom}} = \frac{s_3}{s_3 + 2s_1 + 2s_2} \tag{17}$$

Correction for transmission at internal boundaries: A major difference between Europa and East Antarctica/East-central Greenland is the existence of liquid water beneath an icy layer. When a body wave impinges on a boundary or discontinuity at which the seismic velocity changes, the wave reflects or refracts (Lay and Wallace, 1995). The transmission coefficient T_{coef} is defined as the ratio of transmitted wave amplitude A_{trans} to incident wave amplitude A_{inc}:

$$T_{\text{coef}} = \frac{A_{\text{trans}}}{A_{\text{inc}}}. \tag{18}$$

Subsequently, we use $T_{\mathrm{I}\to\mathrm{II}}$ to denote the transmission coefficient of the P-wave transmitted from material I to II. The A_{ref} parameter in the derived refracted wave scaling law (Eq. 7) already implicitly includes the effect of two transmission coefficients, $T_{\text{ice}\to\text{rock}}$ and $T_{\text{rock}\to\text{ice}}$. However, in the case of teleseismic (PMP) events on Europa, seismic waves go through the layer of ice, ocean, and mantle, thus $T_{\text{ice}\to\text{water}}$, $T_{\text{water}\to\text{rock}}$, $T_{\text{rock}\to\text{water}}$, and $T_{\text{water}\to\text{ice}}$ should be accounted for. Therefore, to convert the case of East Antarctica/East-central Greenland to Europa, the following correction factor f_{trans} should be applied:

$$f_{\text{trans}} = \frac{T_{\text{ice}\to\text{water}} T_{\text{water}\to\text{rock}} T_{\text{rock}\to\text{water}} T_{\text{water}\to\text{ice}}}{T_{\text{ice}\to\text{rock}} T_{\text{rock}\to\text{ice}}}. \tag{19}$$

Transmission coefficients depend on layer densities, velocities, and incidence angles. For non-vertical incidence, P-waves generate S-wave conversions due to the shear stress component at the interface (Shearer, 2009; Aki and Richards, 2002), which reduces the P-wave transmission coefficient. For the ice-rock (solid-solid) interfaces in terrestrial ice sheets we calculated the transmission coefficients using the expressions in Aki and Richards (2002). For the ice-water and water-rock boundaries (solid-liquid) we use the expressions derived for the inner-outer core in Tkalčić et al. (2009). Incidence angles above and below internal boundaries were determined from the ray parameter, which is equivalent to using Snell's law. Note that for simplicity the properties of each layer (i.e., ice, water, and rock) are assumed to be the same in both Europa's and Earth's interiors when determining transmission coefficients (values given in Table 2). The combined P-wave transmission from ice-rock-ice ($T_{\text{ice}\rightarrow\text{rock}}T_{\text{rock}\rightarrow\text{ice}}$) for the refracted wave is 0.36 to a good approximation for angles close to the critical angle. The combined refracted PMP-wave transmission coefficient ($T_{\text{ice}\rightarrow\text{water}}T_{\text{water}\rightarrow\text{rock}}T_{\text{rock}\rightarrow\text{water}}T_{\text{water}\rightarrow\text{ice}}$) is plotted in Figure 6f and is maximum for vertical incidence and minimum close to the critical angle, where much of the energy is lost to S-wave conversions and P-wave reflections.

Correction for attenuation: The attenuation for a path length l at frequency f is given by $\exp\left(-\pi l f/vQ\right)$ (Shearer, 2009), so the combined attenuation correction factor for the refracted P-wave is:

$$f_{\text{atten}} = \exp\left[-\left(\frac{2\pi f s_1}{v_1 Q_1}\right) + \left(\frac{2\pi f x_i}{v_1 Q_{1\oplus}}\right) - \left(\frac{2\pi f s_2}{v_2 Q_2}\right) - \left(\frac{\pi f s_3}{v_3 Q_3}\right) + \left(\frac{\pi f s_3}{v_3 Q_{3\oplus}}\right)\right] \tag{20}$$

where $Q_{1\oplus}$ is the Q_p in the terrestrial ice sheet and $Q_{3\oplus}$ is the Q_p in the terrestrial crust. We assume $Q_{1\oplus}$=65 (Clee et al., 1969) and $Q_{3\oplus}$=1350 (Dziewonski and Anderson, 1981). The factors of 2 in the exponents are to account for upward and downward ray path segments. The negative exponents are the attenuation due to Europa's layers and the positive exponents are to correct for terrestrial attenuation so that predicted amplitudes are not attenuated twice. For an ice crust thickness of 20 km, as listed in Table 2, $s_1 \gg x_i$ and x_i can be neglected to give:

$$f_{\text{atten}} = \exp\left[-\left(\frac{2\pi f s_1}{v_1 Q_1}\right) - \left(\frac{2\pi f s_2}{v_2 Q_2}\right) - \left(\frac{\pi f s_3}{v_3 Q_3}\right) + \left(\frac{\pi f s_3}{v_3 Q_{3\oplus}}\right)\right] \tag{21}$$

For the nominal Q model, $Q_3 = Q_{3\oplus}$, so the last two terms will cancel.

3.2.6. Overall relations between crater diameter and seismic amplitude

The key relations developed so far can be summarised as follows, where all quantities are in SI units:

- The relation between crater diameter D (metres) and impactor energy E (Joules) is given by:

$$D = \alpha_\oplus E^\beta \left(\frac{g_\oplus}{g}\right)^{1/4} = \alpha E^\beta \tag{22}$$

- The amplitude $A'_{E_{\text{impact}}}$ (ms^{-1}) of the direct P-wave travelling though Europa's ice crust at great circle distance x (metres) with a dominant frequency f is given by:

$$A'_{E_{\text{impact}}} = sA'_{\text{ref}} \left(\frac{x}{x_{\text{ref}}}\right)^{-1} \left(\frac{E}{E_{\text{ref}}}\right)^c \exp\left(-\frac{\pi f x}{v_1 Q_1}\right) \exp\left(+\frac{\pi f x_{\text{ref}}}{v_i Q_{1\oplus}}\right), \tag{23}$$

- The amplitude $A_{E_{\text{impact}}}$ (ms^{-1}) of the refracted PMP-wave travelling though Europa's ice crust, water ocean, and rocky mantle with a dominant frequency f is given by:

$$A_{E_{\text{impact}}} = sA_{\text{ref}} \left(\frac{s_3(x)}{x_{\text{ref}}}\right)^b \left(\frac{E}{E_{\text{ref}}}\right)^c f_{\text{trans}} f_{\text{geom}} f_{\text{atten}} \tag{24}$$

$$f_{\text{geom}} = \frac{s_3}{s_3 + 2s_1 + 2s_2} \tag{25}$$

$$f_{\text{trans}} = \frac{T_{\text{ice}\to\text{water}} T_{\text{water}\to\text{rock}} T_{\text{rock}\to\text{water}} T_{\text{water}\to\text{ice}}}{T_{\text{ice}\to\text{rock}} T_{\text{rock}\to\text{ice}}} \tag{26}$$

$$f_{\text{atten}} = \exp\left[-\left(\frac{2\pi f s_1}{v_1 Q_1}\right) - \left(\frac{2\pi f s_2}{v_2 Q_2}\right) - \left(\frac{\pi f s_3}{v_3 Q_3}\right) + \left(\frac{\pi f s_3}{v_3 Q_{3\oplus}}\right)\right] \tag{27}$$

where for a given source-receiver distance $x = r_1\Delta$, the path lengths in each layer $s_{1,2,3}$ and transmission coefficients are derived by interpolating a forward model ray tracing tabulation.

Parameters are summarised in Tables 1 and 2, where major error sources are combined using the formulae in Bevington and Robinson (1992), giving an overall factor of five error in the predicted amplitudes. Note, as the parameters derived here contain considerable uncertainty, they are only appropriate for providing order of magnitude level estimates of predicted seismic impact signals.

While we have quantified potential error sources as much as possible, there are also extra uncertainties related to the internal structure. The largest extra uncertainty source is due to the lack of constraint on the icy crust and mantle Q. This is dealt with explicitly by using three interior Q models (Table 2), which cover the range of plausible attenuation properties. It will later become apparent that the effect of this uncertainty is larger than that due to the scaling relation uncertainties.

Ice crust thickness is also somewhat uncertain at present. If a 5 km crust thickness is assumed instead of 20 km, then predicted amplitudes of the PMP refracted arrivals are approximately a factor of two higher for a given impact. The amplitudes of the direct P-waves are unaffected as these propagate laterally and remain within the ice crust.

We have neglected possible scattering effects in this study, which could also have an effect on seismogram amplitude. The most likely place for scatters is in the rigid conductive stagnant ice lid. However, Cammarano et al. (2006) and Panning et al. (2006) predict that strong scattering effects are not expected on Europa because this lid is relatively thin. Furthermore, Nimmo et al. (2003) have also shown that ice flow in the top kilometre will remove all porosity, which is the most likely candidate for scattering effects. Since seismometers on East Antarctica/East-central Greenland were established on somewhat porous icy surfaces, resultant amplitudes on Europa could be slightly larger than predicted by Eqs. 23–27.

A final source of uncertainty is the frequency content of the impact events. Gudkova et al. (2011) note a roll off in lunar impact events above 2 Hz, which they suggest is related to the finite crater excavation timescale, compared to more impulsive explosive events which retain higher frequencies. Therefore, we consider 2 Hz as a representative frequency for the impact generated signal for the rest of this study. This frequency overlaps with the analog data and provides a realistic central frequency.

Figure 7 shows predicted amplitudes of the direct P and refracted PMP-waves assuming a 2Hz signal for 1, 10, and 100 m diameter craters using the scaling relations in Eqs. 22–27 for low-, nominal-, and high-Q interior models. At large offsets the uncertainty in Q introduces extreme uncertainties of up to four orders of magnitude in the predicted amplitudes. However, these uncertainties are extremely conservative and cover all plausible interior attenuation models. We regard the nominal-Q case as our best estimate of seismic amplitudes.

4. Number of detectable impacts

Thus far, seismic amplitudes of direct P-waves and refracted PMP-waves for a given impact energy have been derived. We now compare these predicted amplitudes to the threshold at which a representative seismometer could potentially identify seismic signals. This threshold is either controlled by levels of ambient noise or seismometer performance.

Both ambient and seismometer noise are typically specified in terms of power spectral density (PSD) with units $\mathrm{m^2 s^{-4}\,Hz^{-1}}$ (Peterson, 1993; Havskov and Alguacil, 2004). However, it is also common to report the square root of the PSD, which we adopt here. Before considering likely instrument and ambient noise levels it is useful to discuss how the power spectral density P_a relates to seismogram amplitude. First, let the acceleration noise spectral density p_a be defined by:

$$p_a = \sqrt{P_a} \tag{28}$$

so that p_a has units $\mathrm{ms^{-2}\,Hz^{-1/2}}$. At dominant frequency f the velocity noise spectral density p_v is given by:

$$p_v = \frac{p_a}{2\pi f} \tag{29}$$

The peak noise amplitudes for acceleration n_a and velocity n_v, as would be measured from a seismogram, in frequency band f_1–f_2 are then given by (Havskov and Alguacil, 2004):

$$n_a = 1.25 p_a \sqrt{f_2 - f_1} \tag{30}$$

$$n_v = 1.25 p_v \sqrt{f_2 - f_1} \tag{31}$$

Earth seismic noise is dominated by oceanic waves, wind, and anthropogenic sources, which have a strong dependence on frequency (Peterson, 1993; McNamara and Buland, 2004). For example, at periods of around 5 seconds, in the microseismic noise band, the dominant noise source is ocean waves, whereas at higher frequencies wind and anthropogenic noise dominate. Earth is a high seismic noise environment, with a quiet site having a noise level of $\sim 10^{-8}$ ms^{-2} Hz$^{-1/2}$ at 2 Hz and a noisy site having a noise level of $\sim 10^{-6}$ ms^{-2} Hz$^{-1/2}$ at 2 Hz (Peterson, 1993).

On Europa, atmospheric noise can be effectively ruled out as the atmosphere is too tenuous (McGrath et al., 2004). Wave noise and anthropogenic sources will also be absent. Ambient noise is expected to be dominated by frequent small-scale fracturing in the rigid outer ice shell driven by diurnal stress variations (Lee et al., 2003). This is very difficult to accurately predict *a priori* as it depends on crack spacing, recurrence interval, and crack depth, all of which are highly uncertain. For a crack spacing of 100 m, 1 minute recurrence intervals, and 50 m crack depths, Lee et al. (2003) predict a peak noise level of 35 decibels below 1 μms^{-1} ($\sim 2\times10^{-8}$ ms^{-1}) in the 1–4 Hz frequency band. This is equivalent to a noise spectral density of p_a=10^{-7} ms^{-2} Hz$^{-1/2}$ at 2 Hz, which falls between high and low noise sites on Earth. Lee et al. (2003) regard this as a worst case scenario, with all cracks active and maximum diurnal stress.

Seismometer sensitivity is another limiting factor to impact detection. Kovach and Chyba (2001) summarise the performance of Apollo and early martian seismometer attempts, with application to Europa. However, the NASA InSight mission seismometers allow more current comparisons; specifically the Very Broad Band (VBB) seismometer (Lognonne et al., 2014; Dandonneau et al., 2013) and the Short Period (SP) seismometer (Pike et al., 2005; Delahunty and Pike, 2014). The VBB noise level at 2 Hz is 10^{-9} ms^{-2} Hz$^{-1/2}$ and that of the SP is 10^{-8} ms^{-2} Hz$^{-1/2}$ (Lognonne et al., 2014). Due to its compact size, an SP-like seismometer is perhaps a more likely instrument to incorporate into a future Europa lander and it is plausible that future development could lead to further reductions in noise level. In any case, based on current instrumentation, a seismometer sensitivity in the 10^{-9}–10^{-8} ms^{-2} Hz$^{-1/2}$ range seems reasonably achievable.

An impact event will be detectable if it produces a P or PMP amplitude greater than or equal to the noise level. Because of the gross uncertainty surrounding current ambient noise level estimates on Europa, we consider two noise level end members: (1) *low noise case* where the seismometer sensitivity is the limiting factor, p_a=3×10^{-9} ms^{-2} Hz$^{-1/2}$ based on an SP-like instrument with modest future development (T. Pike *pers. comm.*); and (2) *high noise case* where crack noise is the limiting factor, p_a=10^{-7} ms^{-2} Hz$^{-1/2}$ (Lee et al., 2003).

Figure 8 shows the maximum source-receiver distance $x_{\max}(D)$ and angular offset $\Delta_{max}(D)$ where an impact would be detectable, as a function of crater diameter D, for both high and low noise cases and all three Q models. We calculate detection ranges of direct P-waves and refracted PMP-waves separately and assume a frequency bandwidth of 1–16 Hz for calculating the peak seismometer noise levels (see Table 1).

The maximum angular detection offset $\Delta_{max}(D)$ can be converted into the fractional area of Europa f_a over which the impact is detectable using simple geometry (Teanby and Wookey, 2011):

$$f_a(D) = \frac{1}{2}\left[1 - \cos\left(\Delta_{max}(D)\right)\right], \tag{32}$$

Finally the number of detectable impacts per year for each crater diameter bin $N_{det}(D)$ can be derived by multiplying the detectable fraction by the crater production function:

$$N_{det}(D) = f_a(D)N(D). \tag{33}$$

where $N(D)$ is the incremental cratering rate in $\sqrt{2}$-width bins centred on diameter D (Hartmann, 2005). The incremental crater production functions are derived from the cumulative impactor rates in Fig. 1 assuming an impact velocity of $v = 2.6 \times 10^4$ ms^{-1} and an impactor density of ρ_i=600 kg m^{-3} (Zahnle et al., 2003). The nominal production function $N(D)$ is given in Table 3.

The number of detections for each noise case are shown in Fig. 8, with numerical values given in Table 3. For the high noise case the predicted number of impact-generated direct P-waves detected is 0.002–1 per year and the number of PMP-waves detected is $7{\times}10^{-9}$–0.01 per year, where the uncertainty ranges span estimates from all Q models and include all error sources. For the low noise case the predicted number of impact-generated direct P-waves detected is 0.05–20 per year and the number of PMP-waves detected is $4{\times}10^{-6}$–1 per year. The dominant source of uncertainty in these estimates is due to the choice of Q model, especially for the mantle, which results in up to six orders of magnitude uncertainty in the PMP detection rates.

For our nominal Q model, the high noise case predicts 0.002–0.4 direct P and $6{\times}10^{-6}$–$2{\times}10^{-3}$ PMP detections per year, whereas the low noise case predicts 0.1–5 direct P and $9{\times}10^{-4}$–0.2 PMP detections per year.

The most frequent detections of P-waves are for very small craters with diameters D$\sim$1 m, at the lower cut off of our extrapolation of Levison et al.

(2000)'s impact rate curve. These small events occur within a few hundred kilometres of the seismometer and may be detectable up to a few times per year. It is possible that many more very small impacts, with craters smaller than 1 m, could be detected on more local scales (<10–100 km) if extrapolation to even smaller impactor sizes is valid. However, impactors much smaller than a millimetre are unlikely to follow this distribution as such small particles will be removed by Poynting-Robertson drag (Grun et al., 1985). Also, while small events could be used to probe the ice crust layer, they would not be energetic enough to probe the deep interior.

PMP-waves, which would probe the deep interior, are much harder to detect than direct P-waves. Nominally, an impact event in which a seismometer could detect a refracted PMP-wave would occur only once every 10–10^5 years.

The most optimistic case for impact detection is the high-Q interior model, corresponding to a cold interior, with noise limited by the seismometer performance (low noise). In this case there would be 0.3–20 direct P waves and 0.006–1 PMP waves detected per year. Therefore, even for optimistic assumptions our results suggest that probing the deep interior and mantle using impacts will be challenging with any reasonable landed mission duration.

5. Discussion and conclusions

In this paper we predict detection rates of seismic waves induced by meteorite impacts on Europa for a range of internal models and noise levels. To obtain impact detection rates we derived amplitude scaling relations as a function of distance and crater diameter using analogue explosive experiments in terrestrial ice sheets, which could potentially be applied to other icy satellites. These relations were combined with extrapolated impactor rate distributions, instrument sensitivity, and noise estimates to give detection rate estimates. Seismic waves were classified into two phases: direct P-waves passing only through the ice crust; and refracted PMP-waves passing through the ice crust, ocean layer, and mantle.

For a nominal interior attenuation model, we predict that only 0.002–5 direct P-waves would be detected per year by a single seismic station. Refracted PMP-waves will be even more difficult to detect, with a nominal detection rate of 6×10^{-6}–0.2 per year. Furthermore, current Europa lander scenarios limit surface operations to $\sim$30 days because of the harsh radiation environment (Pappalardo et al., 2013), suggesting fewer than one instance of any type of impact induced signal during the landed phase of a mission. Therefore, we conclude that impacts should not be considered a reliable seismic source for future exploration of Europa. Future seismic exploration of Europa should primarily rely on surface faulting and cracking, which have the potential to provide much more frequent and energetic sources (Lee et al., 2003; Panning et al., 2006).

However, we caution that our detection rate estimates contain considerable uncertainties. The most important uncertainty source is Europa's internal attenuation properties, for which we considered a nominal case and two extreme end member cases. In this paper we assume an ice crust thickness of 20 km. Thinner crusts would be slightly more favourable for detection of mantle refracted waves as less ice attenuation would occur. The magnitude of this effect would depend on the ice attenuation properties, but for a 5 km ice crust and a nominal Q=65 the refracted amplitudes would be increased by roughly a factor of two. However, this uncertainty has less effect on predicted detection rates than the large uncertainty in interior attenuation properties. Other major sources of uncertainty are the small impactor source population and ambient noise levels, which we consider in turn below:

Impactor source population: When estimating the number of detectable impacts, the small impactor rate is one of the most important factors. Unfortunately, most global-scale measurements of Europa's crater population are for larger craters and extrapolation to small impacts is required. Although small craters have been investigated locally in some regions, the power index of their differential size-frequency distributions are highly variable due to the effect of secondaries (Bierhaus et al., 2005). Therefore, for the current small cratering rate on Europa, we use the relative impact probability of Europa compared to Jupiter of $P_{\mathrm{EC}} = 6.6 \times 10^{-5}$ (Zahnle et al., 2003) and an extrapolation of the Jupiter impact model from Levison et al. (2000), which is the most consistent with recent impact flash observations (Hueso et al., 2013). This gives us reasonably well constrained cratering rates for $\sim$100 m scale craters ($\sim$10 m diameter impactors). In this paper, we have effectively extrapolated the impactor diameter population by three orders of magnitude from $\sim$10 m down to 0.01 m by using the dynamical model of Levison et al. (2000). These small diameters are currently unconstrained by observations and this extrapolation may be somewhat questionable. In fact, the most frequent detections are for the smallest 1 m size craters close to the seismometer, so this extrapolation becomes important when considering overall detection rates or very local events. However, it is less important when considering detection of PMP phases, which require much larger craters (D ∼100 m) whose rates are reasonably well constrained.

Therefore, in future missions it will be important to constrain the small impactor flux by observing the surface at high resolution. ESA's JUICE mission, scheduled to launch in 2022 will arrive in the Jupiter system in 2030, perform several Europa flybys and enter orbit around Ganymede in 2032 with end of nominal mission in 2033 (Grasset et al., 2013; ESA, 2014). Selected areas on Ganymede and Europa will be imaged at high resolutions of up to 6 m/pixel. Approximately 0.1% of Ganymede will be imaged at the highest 6 m/pixel resolution, 20% at 100 m/pixel, and global coverage at 400 m/pixel (ESA, 2014). This is at least an order of magnitude improvement over Galileo and will improve our understanding of the small impactor population. However, at these coverage levels, it is unlikely that new craters will be found using differential imaging as has been possible at Mars (Malin et al., 2006; Daubar et al., 2013). For example, at 6 m/pixel resolution, ∼12 m diameter craters (two pixels) may be just discernible. Assuming the Jupiter impactor flux model of Levison et al. (2000) and the relative impact probability on Ganymede of 1.2×10^{-4}, implies ∼10 craters over 12 m diameter per year for the whole of Ganymede, which translates into a probability of less than 1% of seeing a new crater by differential imaging. These odds may improve if new craters cause more widespread ejecta patterns, as observed by Schenk and Ridolfi (2002) for larger craters (D >13 km).

Noise levels: The major noise source on Europa is expected to be tidally induced thermal cracking of the ice shell. Our results show that the nominal noise estimates by Lee et al. (2003) ($\sim 10^{-7}$ ms^{-2} Hz$^{-1/2}$) would swamp any seismic signal from impacts for all but the largest or most local events, although the exact noise levels contains many orders of magnitude uncertainty. Therefore, we have also considered the more tractable seismometer performance as a limiting detection factor. We also note that if ambient noise due to cracking is much higher than $\sim 10^{-9}$ ms^{-2} Hz$^{-1/2}$ then the focus of a seismic mission would be dominated by faulting and surface activity, so an absence of impact seismic source would be less important for studying the internal structure. In terms of an overall seismic study the distinction between signal and noise would be somewhat subjective; low noise would favour impact detection and large isolated faulting events, whereas high noise would favour intrinsic surface activity such as cracking and small scale fracturing.

To summarise, we have presented seismic detectability of meteorite impacts on Europa under reasonable assumptions. In an optimistic case, a few detections of small local impacts may be possible, which will give information on the ice crust, but global-scale impact events refracted through the mantle are very unlikely to be detected by a short duration mission. Our results suggest that fracturing is likely to be the most important source of seismic energy on Europa, with impacts providing a potential secondary seismic source. Our results should be considered order of magnitude only due to the present large uncertainties in small impact rates, internal attenuation, and ambient noise conditions. Despite the gross uncertainties, these results are useful for planning the next generation of outer solar system missions. Further refinement of these estimates would require greater constraints on the small (D <100 m) cratering rater and Europa's internal attenuation properties.

Finally, we note that a seismometer would be an extremely valuable addition to any surface mission. In addition to fault activity it would potentially be able to measure normal modes (ringing) excited by large europa-quakes or crack noise, ocean resonance modes, ambient noise levels and frequency characteristics, and perhaps even cryovolcanic activity.

Acknowledgments

We appreciate thoughtful comments and reviews by Mark Panning and an anonymous reviewer, which significantly improved the manuscript. We also thank H. Katsuragi, K. Tadokoro, J. Wookey and J.-M. Kendall for valuable comments, fruitful discussions, and suggestions. This research has been supported by the exchange study program between Nagoya University and the University of Bristol led by S. Wallis. N. A. Teanby is supported by the UK Space Agency (ST/L000601/1 and ST/N001044/1) and the UK Science and Technology Facilities Council (ST/M007715/1).

References

Aki, K., Richards, P. G., 2002. Quantitative Seismology, 2nd Edition. University Science Books, Sausalito.

Anderson, D. L., Duennebier, F. K., Latham, G. V., Toksäz, M. F., Kovach, R. L., Knight, T. C. D., Lazarewicz, A. R., Miller, W. F., Nakamura, Y., Sutton, G., 1976. The Viking seismic experiment. Science 194, 1318–1321.

Anderson, J. D., Schubert, G., Jacobson, R. A., Lau, E. L., Moore, W. B., Sjogren, W. L., 1998. Europa's differentiated internal structure: Inferences from four Galileo encounters. Science 281, 2019–2022.

Banerdt, W. B., Smrekar, S., Lognonné, P., Spohn, T., Asmar, S. W., Banfield, D., Boschi, L., Christensen, U., Dehant, V., Folkner, W., Giardini, D., Goetze, W., Golombek, M., Grott, M., Hudson, T., Johnson, C., Kargl, G., Kobayashi, N., Maki, J., Mimoun, D., Mocquet, A., Morgan, P., Panning, M., Pike, W. T., Tromp, J., van Zoest, T., Weber, R., Wieczorek, M. A., Garcia, R., Hurst, K., Mar. 2013. InSight: A Discovery Mission to Explore the Interior of Mars. In: Lunar and Planetary Science Conference. Vol. 44 of Lunar and Planetary Inst. Technical Report. p. 1915.

Bentley, C. R., Kohnen, H., 1976. Seismic refraction measurements of internal friction in Antarctic ice. J. Geophys. Res. 81, 1519–1526.

Bevington, P. R., Robinson, D. K., 1992. Data Reduction and Error Analysis for the Physical Science, 2nd Edition. McGraw-Hill, Inc., New York.

Bierhaus, E. B., Chapman, C. R., Merline, W. J., 2005. Secondary craters on Europa and implications for cratered surfaces. Nature 437, 1125–1127.

Bierhaus, E. B., Chapman, C. R., Merline, W. J., Brooks, S. M., Asphaug, E., 2001. Pwyll secondaries and other small craters on Europa. Icarus 153, 264 – 276.

Bills, B. G., Ferrari, A. J., 1977. A lunar density model consistent with topographic, gravitational, librational, and seismic data. Journal of Geophysical Research 82, 1306–1314.

Bray, V. J., 2009. Impact crater formation on the icy Galilean satellites. Ph.D. thesis, Imperial College London, cited data are in Table 7.3.

Bray, V. J., Collins, G. S., Morgan, J. V., Melosh, H. J., Schenk, P. M., 2014. Hydrocode simulation of Ganymede and Europa cratering trends − how thick is Europa's crust? Icarus 231, 394 – 406.

Brunini, A., Di Sisto, R. P., Orellana, R. B., 2003. Cratering rate on the jovian system: the contribution from Hilda asteroids. Icarus 165, 371–378.

Burger, M. H., Wagner, R., Jaumann, R., Cassidy, T. A., 2010. Effects of the External Environment on Icy Satellites. Space Sci. Rev. 153, 349–374.

Cammarano, F., Lekic, V., Manga, M., Panning, M., Romanowicz, B., 2006. Long-period seismology on Europa: 1. physically consistent interior models. Journal of Geophysical Research: Planets 111 (E12), E12009.

Carr, M. H., Belton, M. J. S., Chapman, C. R., Davies, M. E., Geissler, P., Greenberg, R., McEwen, A. S., Tufts, B. R., Greeley, R., Sullivan, R., Head, J. W., Pappalardo, R. T., Klaasen, K. P., Johnson, T. V., Kaufman, J., Senske, D., Moore, J., Neukum, G., Schubert, G., Burns, J. A., Thomas, P., Veverka, J., 1998. Evidence for a subsurface ocean on Europa. Nature 391, 363–365.

Cassen, P., Reynolds, R. T., Peale, S. J., 1979. Is there liquid water on Europa? Geophysical Research Letters 6, 731–734.

Chyba, C., Phillips, C., 2002. Europa as an abode of life. Origins of life and evolution of the biosphere 32, 47–67.

Chyba, C. F., 2000. Energy for microbial life on Europa. Nature 403, 381–382.

Chyba, C. F., Phillips, C. B., 2001. Possible ecosystems and the search for life on Europa. Proceedings of the National Academy of Sciences 98, 801–804.

Clee, T. E., Savage, J. C., Neave, K. G., 1969. Internal friction in ice near its melting point. J. Geophys. Res. 74, 973–980.

Collinson, G., UK Penetrator Consortium, 2008. Planetary Penetrators - The Vanguard for the Future Exploration of the Solar System. Journal of the British Interplanetary Society 61, 198–202.

Crotwell, H. P., Owens, T. J., Ritsema, J., 1999. The TauP Toolkit: Flexible seismic travel-time and ray-path utilities. Seis. Res. Lett. 70, 154–160.

Dandonneau, P.-A., Lognonne, P., Banerdt, W. B., Deraucourt, S., Gabsi, T., Gagnepain-Beyneix, J., Nebut, T., Robert, O., Tillier, S., Hurst, K., Mimoun, D., Christenssen, U., Bierwirth, M., Roll, R., Pike, T., Calcutt, S., Giardini, D., Mance, D., Zweifel, P., Laudet, P., Kerjean, L., Perez, R., Seis Team, 2013. The SEIS InSight VBB Experiment. In: Lunar and Planetary Science Conference. Vol. 44 of Lunar and Planetary Science Conference. p. 2006.

Daubar, I. J., McEwen, A. S., Byrne, S., Kennedy, M. R., Ivanov, B., 2013. The current martian cratering rate. Icarus 225, 506–516.

Delahunty, A., Pike, W., 2014. Metal-armouring for shock protection of mems. Sensors and Actuators A: Physical 215, 36 – 43.

Di Sisto, R. P., Brunini, A., Dirani, L. D., Orellana, R. B., 2005. Hilda asteroids among Jupiter family comets. Icarus 174, 81–89.

Dziewonski, A. M., Anderson, D. L., 1981. Preliminary reference Earth model. Phys. Earth Planet. Int. 25, 297–356.

ESA, 2014. JUpiter ICy moons Explorer: Exploring the emergence of habitable worlds around gas giants ESA Definition Study Report, ESA/SRE(2014)1, available online at <http://sci.esa.int/juice/54994-juice-definition-study-report/>.

Geller, R. J., Ohminato, T., 1994. Computation of synthetic seismograms and their partial derivatives for heterogeneous media with arbitrary natural boundary-conditions using the direct solution method. Geophys. J. Int. 116, 421–446.

Geller, R. J., Takeuchi, N., 1995. A new method for computing highly accurate DSM synthetic seismograms. Geophys. J. Int. 123, 449–470.

Goins, N. R., Dainty, A. M., Toksöz, M. N., 1981. Lunar seismology: The internal structure of the Moon. Journal of Geophysical Research: Solid Earth 86, 5061–5074.

Gowen, R., Smith, A., Fortes, A., Barber, S., Brown, P., Church, P., Collinson, G., Coates, A., Collins, G., Crawford, I., Dehant, V., Chela-Flores, J., Griffiths, A., Grindrod, P., Gurvits, L., Hagermann, A., Hussmann, H., Jaumann, R., Jones, A., Joy, K., Karatekin, O., Miljkovic, K., Palomba, E., Pike, W., Prieto-Ballesteros, O., Raulin, F., Sephton, M., Sheridan, S., Sims, M., Storrie-Lombardi, M., Ambrosi, R., Fielding, J., Fraser, G., Gao, Y., Jones, G., Kargl, G., Karl, W., Macagnano, A., Mukherjee, A., Muller, J., Phipps, A., Pullan, D., Richter, L., Sohl, F., Snape, J., Sykes, J., Wells, N., 2011. Penetrators for in situ subsurface investigations of Europa. Advances in Space Research 48, 725 – 742.

Grasset, O., Dougherty, M. K., Coustenis, A., Bunce, E. J., Erd, C., Titov, D., Blanc, M., Coates, A., Drossart, P., Fletcher, L. N., Hussmann, H., Jaumann, R., Krupp, N., Lebreton, J.-P., Prieto-Ballesteros, O., Tortora, P., Tosi, F., Van Hoolst, T., Apr. 2013. JUpiter ICy moons Explorer (JUICE): An ESA mission to orbit Ganymede and to characterise the Jupiter system. Planetary and Space Science 78, 1–21.

Greeley, R., Chyba, C. F., Head III, J. W., McCord, T. B., McKinnon, W. B., Pappalardo, R. T., Figueredo, P. H., 2004. Geology of Europa. In: Fran Bagenal, Timothy Edward Dowling, W. B. M. (Ed.), Jupiter: The Planet, Satellites and Magnetosphere. Cambridge University Press, Cambridge, pp. 329–362.

Greeley, R., Collins, G. C., Spaun, N. A., Sullivan, R. J., Moore, J. M., Senske, D. A., Tufts, B. R., Johnson, T. V., Belton, M. J. S., Tanaka, K. L., 2000. Geologic mapping of Europa. J. Geophys. Res. E105, 22559–22578.

Greenberg, R., Geissler, P., Hoppa, G., Tufts, B., Durda, D. D., Pappalardo, R., Head, J. W., Greeley, R., Sullivan, R., Carr, M. H., 1998. Tectonic processes on Europa: Tidal stresses, mechanical response, and visible features. Icarus 135, 64 – 78.

Greenberg, R., Hoppa, G. V., Tufts, B., Geissler, P., Riley, J., Kadel, S., 1999. Chaos on Europa. Icarus 141, 263 – 286.

Grun, E., Zook, H. A., Fechtig, H., Giese, R. H., 1985. Collisional balance of the meteoritic complex. Icarus 62, 244–272.

Gudkova, T. V., Lognonné, P., Gagnepain-Beyneix, J., 2011. Large impacts detected by the Apollo seismometers: Impactor mass and source cutoff frequency estimations. Icarus 211, 1049–1065.

Hartmann, W. K., 2005. Martian cratering 8: Isochron refinement and the chronology of Mars. Icarus 174 (2), 294 – 320.

Havskov, J., Alguacil, G., 2004. Instrumentation in Earthquake Seismology. Springer, Netherlands.

Holsapple, K. A., 2015. Crater sizes from explosions or impacts. Available online at <http://keith.aa.washington.edu/craterdata/scaling/usermanual.html>.

Holsapple, K. A., Schmidt, R. M., 1982. On the scaling of crater dimensions: 2. impact processes. Journal of Geophysical Research: Solid Earth 87, 1849–1870.

Hoppa, G. V., Tufts, B. R., Greenberg, R., Geissler, P. E., 1999. Formation of cycloidal features on Europa. Science 285, 1899–1902.

Horedt, G., Neukum, G., 1984. Comparison of six crater-scaling laws. Earth, Moon, and Planets 31, 265–269.

Hueso, R., Pérez-Hoyos, S., Sánchez-Lavega, A., Wesley, A., Hall, G., Go, C., Tachikawa, M., Aoki, K., Ichimaru, M., Pond, J. W. T., Korycansky, D. G., Palotai, C., Chappell, G., Rebeli, N., Harrington, J., Delcroix, M., Wong, M., de Pater, I., Fletcher, L. N., Hammel, H., Orton, G. S., Tabe, I., Watanabe, J., Moreno, J. C., 2013. Impact flux on Jupiter: From superbolides to large-scale collisions. A&A 560, A55.

Iijima, Y., Kato, M., Arakawa, M., Maeno, N., Fujimura, A., Mizutani, H., 1995. Cratering experiments on ice: Dependence of crater formation on projectile materials and scaling parameter. Geophysical Research Letters 22, 2005–2008.

Ikami, A., Kaminuma, K., Ichinose, Y., 1981. Upper crustal structure of Sôya coast, Antarctica, revealed by explosion seismology. Nankyoku Siryô (Antarct. Rec.) 71, 58–63.

Ito, K., Ikami, A., 1984. Amplitudes of seismic waves on ice sheet in east Antarctica. Mem. Natl Inst. Polar Res. Ser. C, Earth sciences 15, 36–42.

Kanamori, H., 1977. Energy-release in great earthquakes. J. Geophys. Res. 82, 2981–2987.

Katsuragi, H., 2015. Physics of Soft Impact and Cratering. Springer, Tokyo.

Kawakami, S.-I., Mizutani, H., Takagi, Y., Kato, M., Kumazawa, M., 1983. Impact experiments on ice. Journal of Geophysical Research: Solid Earth 88, 5806–5814.

Kivelson, M. G., Khurana, K. K., Russell, C. T., Volwerk, M., Walker, R. J., Zimmer, C., 2000. Galileo magnetometer measurements: A stronger case for a subsurface ocean at Europa. Science 289, 1340–1343.

Kohler, W. M., Fuis, G. S., 1992. Empirical dependence of seismic ground velocity on the weight of explosives, shotpoint site condition, and recording distance for seismic-refraction data. Bulletin of the Seismological Society of America 82, 2032–2044.

Kovach, R. L., Chyba, C. F., 2001. Seismic detectability of a subsurface ocean on Europa. Icarus 150, 279 – 287.

Kuskov, O., Kronrod, V., 2005. Internal structure of Europa and Callisto. Icarus 177, 550 – 569.

Kuskov, O. L., Kronrod, V. A., 2001. Core sizes and internal structure of Earth's and Jupiter's satellites. Icarus 151, 204 – 227.

Lange, M. A., Ahrens, T. J., 1987. Impact experiments in low-temperature ice. Icarus 69, 506–518.

Lay, T., Wallace, T. C., 1995. Modern global seismology. Academic Press, San Diego, California.

Lee, S., Zanolin, M., Thode, A. M., Pappalardo, R. T., Makris, N. C., 2003. Probing Europa's interior with natural sound sources. Icarus 165, 144 – 167.

Leith, A. C., McKinnon, W. B., 1996. Is there evidence for polar wander on Europa? Icarus 120, 387 – 398.

Levison, H. F., Duncan, M. J., Zahnle, K., Holman, M., Dones, L., 2000. Planetary impact rates from ecliptic comets. Icarus 143, 415 – 420.

Lognonne, P., Banerdt, W., Pike, T., Giardini, D., Christensen, U., Banfield, D., Mimoun, D., Laudet, P., de Raucourt, S., Bierwirth, M., Zweifel, P., Calcutt, S., Hurst, K., Bruce, C., 2014. SEIS/INSIGHT and Mars seismology: Development status and focus on the Impact detection. In: EGU General Assembly Conference Abstracts. Vol. 16 of EGU General Assembly Conference Abstracts. p. 12183.

Lognonne, P., Gagnepain-Beyneix, J., Chenet, H., 2003. A new seismic model of the Moon: implications for structure, thermal evolution and formation of the Moon. Earth and Planetary Science Letters 211, 27 – 44.

Malin, M. C., Edgett, K. S., Posiolova, L. V., McColley, S. M., Dobrea, E. Z. N., 2006. Present-day impact cratering rate and contemporary gully activity on Mars. Science 314, 1573–1577.

McCollom, T. M., 1999. Methanogenesis as a potential source of chemical energy for primary biomass production by autotrophic organisms in hydrothermal systems on Europa. Journal of Geophysical Research: Planets 104, 30729–30742.

McEwen, A. S., 1986. Tidal reorientation and the fracturing of Jupiter's moon Europa. Nature 321, 49–51.

McGrath, M. A., Lellouch, E., Strobel, D. F., Feldman, P. D., Johnson, R. E., 2004. Satellite atmospheres. In: Fran Bagenal, Timothy Edward Dowling,

W. B. M. (Ed.), Jupiter: The Planet, Satellites and Magnetosphere. Cambridge University Press, Cambridge, pp. 457–484.

McNamara, D., Buland, R., 2004. Ambient noise levels in the continental United States. Bull. Seism. Soc. Am. 94, 1517–1527.

Melosh, H. J., 1980. Cratering mechanics-observational, experimental, and theoretical. Annual Review of Earth and Planetary Sciences 8, 65–93.

Melosh, H. J., 1989. Impact cratering: A geologic process. Oxford University Press, New York.

Mitri, G., Showman, A. P., 2005. Convective conductive transitions and sensitivity of a convecting ice shell to perturbations in heat flux and tidal-heating rate: Implications for Europa. Icarus 177, 447–460.

Moore, W. B., 2006. Thermal equilibrium in Europa's ice shell. Icarus 180, 141–146.

Nakamura, Y., 1976. Seismic energy transmission in the lunar surface zone determined from signals generated by movement of lunar rovers. Bulletin of the Seismological Society of America 66, 593–606.

Nakamura, Y., 1983. Seismic velocity structure of the lunar mantle. Journal of Geophysical Research: Solid Earth 88, 677–686.

Nakamura, Y., Koyama, J., 1982. Seismic Q of the lunar upper mantle. Journal of Geophysical Research: Solid Earth 87, 4855–4861.

Nimmo, F., Giese, B., Pappalardo, R. T., 2003. Estimates of Europa's ice shell thickness from elastically-supported topography. Geophys. Res. Lett. 30.

Nimmo, F., Manga, M., 2002. Causes, characteristics and consequences of convective diapirism on Europa. Geophys. Res. Lett. 29.

Nimmo, F., Pappalardo, R., Giese, B., 2003. On the origins of band topography, Europa. Icarus 166, 21 – 32.

Nimmo, F., Schenk, P., 2006. Normal faulting on Europa: implications for ice shell properties. J. Struct. Geol. 28, 2194–2203.

Orton, G. S., Fletcher, L. N., Lisse, C. M., Chodas, P. W., Cheng, A., Yanamandra-Fisher, P. A., Baines, K. H., Fisher, B. M., Wesley, A., Perez-Hoyos, S., de Pater, I., Hammel, H. B., Edwards, M. L., Ingersoll, A. P., Mousis, O., Marchis, F., Golisch, W., Sanchez-Lavega, A., Simon-Miller, A. A., Hueso, R., Momary, T. W., Greene, Z., Reshetnikov, N., Otto, E., Villar, G., Lai, S., Wong, M. H., 2011. The atmospheric influence, size and possible asteroidal nature of the July 2009 Jupiter impactor. Icarus 211, 587–602.

Panning, M., Lekic, V., Manga, M., Cammarano, F., Romanowicz, B., 2006. Long-period seismology on Europa: 2. predicted seismic response. Journal of Geophysical Research: Planets 111 (E12), E12008.

Pappalardo, R. T., McKinnon, W. B., Khurana, K. K. (Eds.), 2009. Europa. Space Science Series. University of Arizona Press, Tucson.

Pappalardo, R. T., Senske, D. A., Prockter, L. M., Paczkowski, B., Vance, S., Goldstein, B., Magner, T., Cooke, B., Mar. 2015. Science and Reconnaissance from the Europa Clipper Mission Concept: Exploring Europa's Habitability. In: Lunar and Planetary Science Conference. Vol. 46 of Lunar and Planetary Inst. Technical Report. p. 2673.

Pappalardo, R. T., Vance, S., Bagenal, F., Bills, B. G., Blaney, D. L., Blankenship, D. D., Brinckerhoff, W. B., Connerney, J. E. P., Hand, K. P., Hoehler, T. M., Leisner, J. S., Kurth, W. S., McGrath, M. A., Mellon, M. T., Moore, J. M., Patterson, G. W., Prockter, L. M., Senske, D. A., Schmidt, B. E., Shock, E. L., Smith, D. E., Soderlund, K. M., 2013. Science potential from a Europa lander. Astrobiology 13, 740–773.

Peters, L. E., Anandakrishnan, S., Alley, R. B., Voigt, D. E., 2012. Seismic attenuation in glacial ice: A proxy for englacial temperature. Journal of Geophysical Research: Earth Surface 117, F02008.

Peterson, J., 1993. Observations and modeling of seismic background noise. U.S. Geol. Surv. Tech. Rept. 93-322, 1–95.

Pike, W., Standley, I., Karl, W., Delahunty, A., Calcutt, S., 2010. A Microseismometer for Penetrometer Deployment in the Jupiter System. In: EGU General Assembly Conference Abstracts. Vol. 12 of EGU General Assembly Conference Abstracts. p. 11241.

Pike, W. T., Standley, I. M., Banerdt, W. B., 2005. A High-Sensitivity Broad-Band Seismic Sensor for Shallow Seismic Sounding of the Lunar Regolith. In: Mackwell, S., Stansbery, E. (Eds.), 36th Annual Lunar and Planetary

Science Conference. Vol. 36 of Lunar and Planetary Science Conference. p. 2002.

Reynolds, R. T., Squyres, S. W., Colburn, D. S., McKay, C. P., 1983. On the habitability of Europa. Icarus 56, 246 – 254.

Rhoden, A. R., Hurford, T. A., Manga, M., 2011. Strike-slip fault patterns on Europa: obliquity or polar wander? Icarus 211, 636–647.

Richardson, J. E., Melosh, H. J., Greenberg, R. J., O'Brien, D. P., 2005. The global effects of impact-induced seismic activity on fractured asteroid surface morphology. Icarus 179, 325–349.

Sánchez-Lavega, A., Wesley, A., Orton, G., Hueso, R., Perez-Hoyos, S., Fletcher, L. N., Yanamandra-Fisher, P., Legarreta, J., de Pater, I., Hammel, H., Simon-Miller, A., Gomez-Forrellad, J. M., Ortiz, J. L., García-Melendo, E., Puetter, R. C., Chodas, P., 2010. The impact of a large object on Jupiter in 2009 July. The Astrophysical Journal Letters 715, L155.

Schenk, P. M., Chapman, C. R., Zahnle, K., Moore, J. M., 2004. Ages and interiors: the cratering record of the Galilean satellites. In: Fran Bagenal, Timothy Edward Dowling, W. B. M. (Ed.), Jupiter: The Planet, Satellites and Magnetosphere. Cambridge University Press, Cambridge, pp. 427–456.

Schenk, P. M., Ridolfi, F. J., 2002. Morphology and scaling of ejecta deposits on icy satellites. Geophys. Res. Lett. 29, 31–1.

Schmidt, R. M., Housen, K. R., 1987. Some recent advances in the scaling of impact and explosion cratering. Int. J. Impact Eng. 5, 543–560.

Shearer, P. M., 2009. Introduction to Seismology, 2nd Edition. Cambridge Univ. Press, Cambridge.

Sheehy, M. J., Halley, R., 1957. Measurement of the attenuation of low-frequency underwater sound. J. Acoustical Soc. Am. 29, 464–469.

Shoemaker, E. M., 1983. Asteroid and comet bombardment of the Earth. Annual Review of Earth and Planetary Sciences 11, 461–494.

Shulgin, A., Thybo, H., 2015. Seismic explosion sources on an ice cap - technical considerations. Polar Science 9, 107 – 118.

Sohl, F., Spohn, T., Breuer, D., Nagel, K., 2002. Implications from Galileo observations on the interior structure and chemistry of the Galilean satellites. Icarus 157, 104 – 119.

Spetzler, H., Anderson, D. L., 1968. The effect of temperature and partial melting on velocity and attenuation in a Simple Binary System. J. Geophys. Res. 73, 6051–6060.

Squyres, S., 2011. Vision and Voyages for Planetary Science in the Decade 2013-2022. Committee on the Planetary Science Decadal Survey, National Research Council, available online at <http://www.nap.edu/catalog/13117.html>.

Takeuchi, N., Geller, R. J., Cummins, P. R., 1996. Highly accurate P-SV complete synthetic seismograms using modified DSM operators. Geophys. Res. Lett. 23, 1175–1178.

Teanby, N., 2015. Predicted detection rates of regional-scale meteorite impacts on Mars with the insight short-period seismometer. Icarus 256, 49 – 62.

Teanby, N., Wookey, J., 2011. Seismic detection of meteorite impacts on Mars. Physics of the Earth and Planetary Interiors 186, 70 – 80.

Tkalčić, H., Kennett, B. L. N., Cormier, V. F., 2009. On the inner-outer core density contrast from PKiKP/PcP amplitude ratios and uncertainties caused by seismic noise. Geophysical Journal International 179, 425–443.

Turtle, E. P., Pierazzo, E., 2001. Thickness of a europan ice shell from impact crater simulations. Science 294, 1326–1328.

Vadov, R. A., 2006. Long-range sound propagation in the northwestern region of the Pacific Ocean. Acoustical Physics 52, 377–391.

Wahr, J., Selvans, Z. A., Mullen, M. E., Barr, A. C., Collins, G. C., Selvans, M. M., Pappalardo, R. T., 2009. Modeling stresses on satellites due to non-synchronous rotation and orbital eccentricity using gravitational potential theory. Icarus 200, 188–206.

Zahnle, K., Alvarellos, J. L., Dobrovolskis, A., Hamill, P., 2008. Secondary and sesquinary craters on Europa. Icarus 194, 660 – 674.

Zahnle, K., Dones, L., Levison, H. F., 1998. Cratering rates on the Galilean satellites. Icarus 136, 202 – 222.

Zahnle, K., Schenk, P., Levison, H., Dones, L., 2003. Cratering rates in the outer Solar System. icarus 163, 263–289.

Zahnle, K., Schenk, P., Sobieszczyk, S., Dones, L., Levison, H. F., 2001. Differential cratering of synchronously rotating satellites by ecliptic comets. Icarus 153, 111 – 129.

Parameter	Value	Fractional error	Notes
Crater diameter scaling relation: $D = \alpha_\oplus E^\beta \left(\frac{g_\oplus}{g}\right)^{0.25}$			
$\alpha_\oplus$	1.82×10^{-2}	$\frac{\sigma_{\alpha_\oplus}}{\alpha_\oplus} = 0.39$	Earth value fitted to experimental/simulation data in Fig. 2
β	0.29	$\frac{\sigma_\beta}{\beta} = 0.0069$	Power index fitted to data in Fig. 2
Amplitude scaling relation for explosions in rock/ice:			
A_{ref} †	1.45×10^{-5} ms^{-1}	$\frac{\sigma_{A_{\text{ref}}}}{A_{\text{ref}}} = 2.45$	Refracted wave amplitude; 1000 kg TNT explosion in rock/ice at 10 km (Teanby, 2015)
A'_{ref}	3.0×10^{-5} ms^{-1}	$\frac{\sigma_{A'_{\text{ref}}}}{A'_{\text{ref}}} = 3.0$	Direct wave amplitude; 1000 kg TNT explosion in ice at 10 km
b	-1.60	$\frac{\sigma_b}{b} = 0.023$	Distance power law index in Fig. 3 (Teanby, 2015)
c	0.5	-	Energy power law index in Fig. 3 (Teanby, 2015)
s	0.099	$\frac{\sigma_s}{s} = 3.82$	Scaling parameter from explosions to impacts (Teanby, 2015)
x_{ref}	1×10^4 m	-	Reference distance (10 km)
E_{ref}	4.18×10^9 J	-	Reference energy ($\equiv$ 1000 kg TNT)
$Q_{1\oplus}$	65	-	Assumed Q_p in terrestrial ice sheets (Clee et al., 1969)
$Q_{3\oplus}$	1350	-	Assumed Q_p in Earth's crust (Dziewonski and Anderson, 1981)
$T_{\text{ice}\to\text{rock}\to\text{ice}}$	0.34	-	P-wave transmission coefficient for terrestrial ice sheets close to critical angle.
Constants:			
q	4.18×10^6 J kg^{-1}	-	Specific energy of TNT (Shoemaker, 1983)
r_1	1569 km	-	Europa radius
R	6371 km	-	Earth radius
g	1.31 ms^{-2}	-	Europa gravity
$g_\oplus$	9.81 ms^{-2}	-	Earth gravity
f_1, f_2	1, 16 Hz	-	Nominal frequency range of impact energy
f_0	2 Hz	-	Nominal frequency of impact energy
Low noise case (instrument sensitivity limited):			
p_a	3×10^{-9} ms^{-2}Hz$^{-1/2}$	-	Acceleration spectral density
p_v	2.4×10^{-10} ms^{-1}Hz$^{-1/2}$	-	Velocity spectral density (Eq. 29)
n_v	1.2×10^{-9} ms^{-1}	-	Peak velocity noise (Eq. 31)
High noise case (crack noise limited):			
p_a	10^{-7} ms^{-2}Hz$^{-1/2}$	-	Acceleration spectral density
p_v	8.0×10^{-9} ms^{-1}Hz$^{-1/2}$	-	Velocity spectral density (Eq. 29)
n_v	3.9×10^{-8} ms^{-1}	-	Peak velocity noise (Eq. 31)
		Total $\frac{\sigma_A}{A} \approx 5$	Total fractional amplitude error from major uncertainties

Table 1: Summary of scaling law parameters discussed in the main text and fractional errors. The total fractional amplitude error $\frac{\sigma_A}{A}$ is obtained by assuming independence of each parameter and summing the variances using the error propagation expressions in Bevington and Robinson (1992). For the overall seismogram amplitude relationships (Eqs. 23, 24–27), the dominant uncertainty is caused by s, A_{ref}, and A'_{ref}. †A_{ref} is related to a_0 in Teanby (2015) by $A_{\text{ref}} = a_0(x_{\text{ref}}/1000)^b(E_{\text{ref}}/q)^c$, where $a_0 = 1.825 \times 10^{-5}$, 1000 converts metres to km, and q converts Joules to Kg TNT.

Layer	Depth Range (km)	v_p ($\mathrm{km\,s^{-1}}$)	v_s ($\mathrm{km\,s^{-1}}$)	Density ($\mathrm{g\,cm^{-3}}$)	Q_p (low-Q)	Q_p (nominal-Q)	Q_p (high-Q)
Ice crust	0–20	4.00	2.00	1.00	20	65	200
Ocean	20–123	1.55	-	1.10	5000	5000	5000
Mantle	123–1092	8.20	4.73	3.40	225	1350	22500
Core	1092-1560	5.25	3.03	8.15	190	190	190

Table 2: Simplified interior models. Velocities, densities, and layer boundaries are based on the cold pyrolitic case of Cammarano et al. (2006) with a pure iron core. The three Q_p attenuation models cover the suspected range of properties in Europa's interior and are discussed further in the main text (Section 3.2.1).

D	$N(D)$	N_{det} (yr^{-1})											
		Low Q				*Nominal Q*				*High Q*			
		High noise case		*Low noise case*		*High noise case*		*Low noise case*		*High noise case*		*Low noise case*	
(m)	(yr^{-1})	P-wave	PMP-wave	P-wave	PMP-wave	P-wave	PMP-wave	P-wave	PMP-wave	P-wave	PMP-wave	P-wave	PMP-wave
1.00	1.0×10^{3}	5.3×10^{-3}	-	1.0×10^{-1}	-	3.9×10^{-3}	-	3.3×10^{-1}	-	2.7×10^{-3}	-	8.2×10^{-1}	-
1.41	4.7×10^{2}	4.4×10^{-3}	-	6.3×10^{-2}	-	4.4×10^{-3}	-	2.3×10^{-1}	-	3.9×10^{-3}	-	6.8×10^{-1}	-
2.00	2.1×10^{2}	3.7×10^{-3}	-	3.9×10^{-2}	-	4.9×10^{-3}	-	1.6×10^{-1}	-	5.6×10^{-3}	-	5.7×10^{-1}	-
2.83	9.6×10^{1}	3.2×10^{-3}	-	2.4×10^{-2}	-	5.7×10^{-3}	-	1.1×10^{-1}	-	7.7×10^{-3}	-	4.5×10^{-1}	-
4.00	4.3×10^{1}	2.2×10^{-3}	-	1.3×10^{-2}	-	4.6×10^{-3}	-	6.5×10^{-2}	-	7.8×10^{-3}	-	2.9×10^{-1}	-
5.66	2.0×10^{1}	1.6×10^{-3}	-	7.7×10^{-3}	-	4.2×10^{-3}	-	4.1×10^{-2}	-	9.5×10^{-3}	-	2.0×10^{-1}	-
8.00	8.8×10^{0}	9.3×10^{-4}	-	4.1×10^{-3}	-	2.9×10^{-3}	-	2.3×10^{-2}	-	7.8×10^{-3}	-	1.2×10^{-1}	-
11.31	4.0×10^{0}	5.6×10^{-4}	-	2.2×10^{-3}	-	2.1×10^{-3}	-	1.3×10^{-2}	-	6.4×10^{-3}	-	7.0×10^{-2}	-
16.0	1.8×10^{0}	3.4×10^{-4}	-	1.2×10^{-3}	-	1.4×10^{-3}	-	7.3×10^{-3}	-	5.2×10^{-3}	-	4.2×10^{-2}	-
22.63	8.1×10^{-1}	2.1×10^{-4}	-	6.3×10^{-4}	-	9.5×10^{-4}	-	4.0×10^{-3}	-	3.9×10^{-3}	-	2.4×10^{-2}	-
32.00	3.6×10^{-1}	1.1×10^{-4}	-	3.2×10^{-4}	-	5.7×10^{-4}	-	2.2×10^{-3}	-	2.6×10^{-3}	-	1.3×10^{-2}	3.6×10^{-3}
45.25	1.6×10^{-1}	6.3×10^{-5}	-	1.7×10^{-4}	-	3.4×10^{-4}	-	1.1×10^{-3}	5.8×10^{-4}	1.7×10^{-3}	-	7.3×10^{-3}	6.0×10^{-3}
64.00	7.4×10^{-2}	3.5×10^{-5}	-	8.7×10^{-5}	-	2.0×10^{-4}	-	6.1×10^{-4}	1.5×10^{-3}	1.1×10^{-3}	-	4.0×10^{-3}	1.1×10^{-2}
90.51	3.3×10^{-2}	1.9×10^{-5}	-	4.4×10^{-5}	-	1.1×10^{-4}	-	3.2×10^{-4}	1.7×10^{-3}	6.3×10^{-4}	-	2.1×10^{-3}	2.9×10^{-2}
128.00	1.5×10^{-2}	1.0×10^{-5}	-	2.2×10^{-5}	-	6.3×10^{-5}	-	1.6×10^{-4}	1.9×10^{-3}	3.7×10^{-4}	-	1.1×10^{-3}	1.3×10^{-2}
181.02	6.8×10^{-3}	5.4×10^{-6}	-	1.1×10^{-5}	-	3.5×10^{-5}	-	8.4×10^{-5}	6.0×10^{-3}	2.1×10^{-4}	-	5.8×10^{-4}	6.0×10^{-3}
256.00	3.1×10^{-3}	2.8×10^{-6}	-	5.6×10^{-6}	1.7×10^{-5}	1.9×10^{-5}	-	4.3×10^{-5}	2.7×10^{-3}	1.2×10^{-4}	3.9×10^{-5}	3.0×10^{-4}	2.7×10^{-3}
362.04	1.4×10^{-3}	1.4×10^{-6}	-	2.8×10^{-6}	1.7×10^{-5}	1.0×10^{-5}	9.3×10^{-6}	2.2×10^{-5}	1.2×10^{-3}	6.4×10^{-5}	6.4×10^{-5}	1.5×10^{-4}	1.2×10^{-3}
512.00	6.2×10^{-4}	7.4×10^{-7}	-	1.4×10^{-6}	1.4×10^{-5}	5.2×10^{-6}	1.5×10^{-5}	1.1×10^{-5}	5.5×10^{-4}	3.4×10^{-5}	1.4×10^{-4}	7.8×10^{-5}	5.5×10^{-4}
724.08	2.8×10^{-4}	3.8×10^{-7}	-	6.9×10^{-7}	1.0×10^{-5}	2.7×10^{-6}	1.7×10^{-5}	5.5×10^{-6}	2.5×10^{-4}	1.8×10^{-5}	2.5×10^{-4}	3.9×10^{-5}	2.5×10^{-4}
1024.00	1.4×10^{-4}	1.9×10^{-7}	-	3.4×10^{-7}	6.8×10^{-6}	1.4×10^{-6}	1.9×10^{-5}	2.7×10^{-6}	1.1×10^{-4}	9.6×10^{-6}	1.1×10^{-4}	2.0×10^{-5}	1.1×10^{-4}
1448.15	5.7×10^{-5}	9.6×10^{-8}	-	1.7×10^{-7}	4.4×10^{-6}	7.2×10^{-7}	5.0×10^{-5}	1.4×10^{-6}	5.0×10^{-5}	5.0×10^{-6}	5.0×10^{-5}	9.8×10^{-6}	5.0×10^{-5}
2048.00	2.6×10^{-5}	4.8×10^{-8}	1.7×10^{-7}	8.1×10^{-8}	2.7×10^{-6}	3.7×10^{-7}	2.3×10^{-5}	6.7×10^{-7}	2.3×10^{-5}	2.6×10^{-6}	2.3×10^{-5}	4.9×10^{-6}	2.3×10^{-5}
2896.31	1.2×10^{-5}	2.4×10^{-8}	1.6×10^{-7}	4.0×10^{-8}	1.7×10^{-6}	1.9×10^{-7}	1.0×10^{-5}	3.3×10^{-7}	1.0×10^{-5}	1.3×10^{-6}	1.0×10^{-5}	2.4×10^{-6}	1.0×10^{-5}
4096.00	5.2×10^{-6}	1.2×10^{-8}	1.3×10^{-7}	1.9×10^{-8}	9.9×10^{-7}	9.4×10^{-8}	4.6×10^{-6}	1.6×10^{-7}	4.6×10^{-6}	6.7×10^{-7}	4.6×10^{-6}	1.2×10^{-6}	4.6×10^{-6}
Total number N_{tot}		2.3×10^{-2}	4.6×10^{-7}	2.6×10^{-1}	7.5×10^{-5}	3.6×10^{-2}	1.5×10^{-4}	9.9×10^{-1}	1.7×10^{-2}	6.7×10^{-2}	7.0×10^{-4}	3.3×10^{0}	7.4×10^{-2}
Upper limit with $1\sigma_{N_{tot}}$		1.7×10^{-1}	1.2×10^{-5}	1.1×10^{0}	1.4×10^{-3}	4.1×10^{-1}	2.2×10^{-3}	5.2×10^{0}	2.3×10^{-1}	9.6×10^{-1}	1.3×10^{-2}	2.3×10^{1}	1.4×10^{0}
Lower limit with $1\sigma_{N_{tot}}$		1.9×10^{-3}	7.2×10^{-9}	5.1×10^{-2}	4.4×10^{-6}	2.4×10^{-3}	6.2×10^{-6}	1.3×10^{-1}	8.8×10^{-4}	4.2×10^{-3}	5.1×10^{-5}	3.3×10^{-1}	6.1×10^{-3}

Table 3: Impact rates and predicted detections, as plotted in Fig. 8. The impact model is based on the extrapolation of Levison et al. (2000). Columns are: D crater diameter bin centre; $N(D)$ incremental cratering rate; $N_{\mathrm{det}}(D)$ number of detectable P/PMP-waves. Results are shown for three Q attenuation models and two different noise cases. Bins are spaced by a factor of $\sqrt{2}$ following Hartmann (2005).

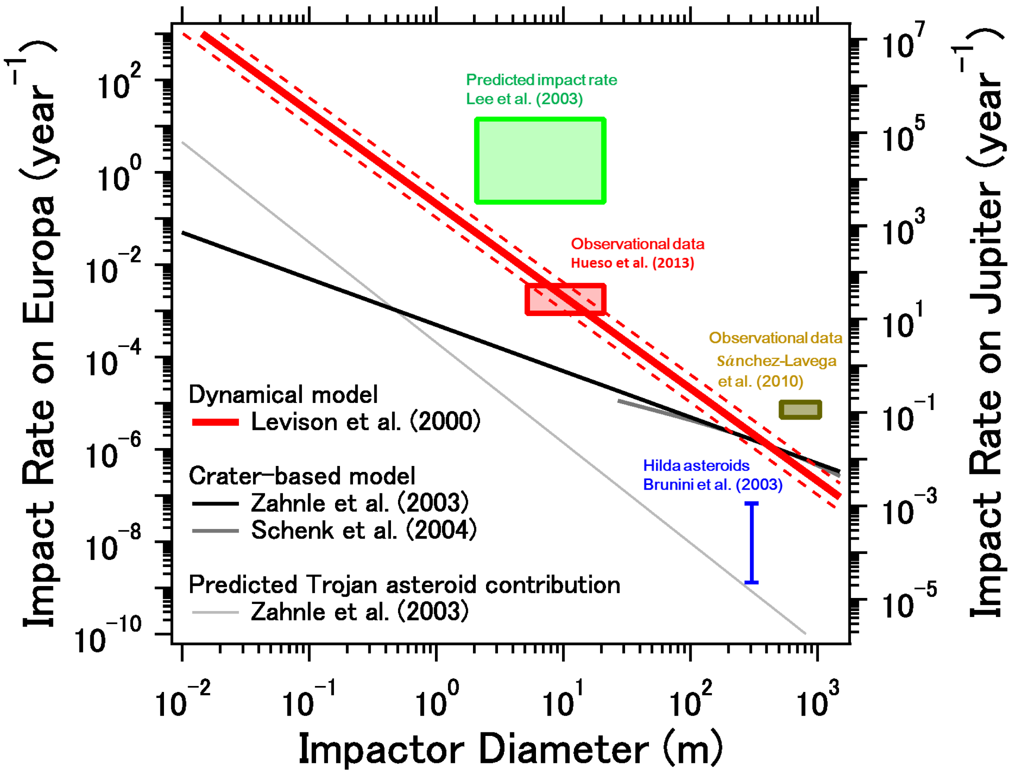

Figure 1: Cumulative impact rate estimates for Europa and Jupiter. An extrapolation of the dynamical model for Jupiter-family comets proposed by Levison et al. (2000) is supported by recent observations of impact flashes into Jupiter (Hueso et al., 2013) and is employed throughout this paper. The contribution from asteroids is predicted to be between one and three orders of magnitude lower than from comets. Note that impact rates on Europa are related to those on Jupiter by using the scale factor $P_{\rm EC} = 6.6 \times 10^{-5}$ (Zahnle et al., 2003).

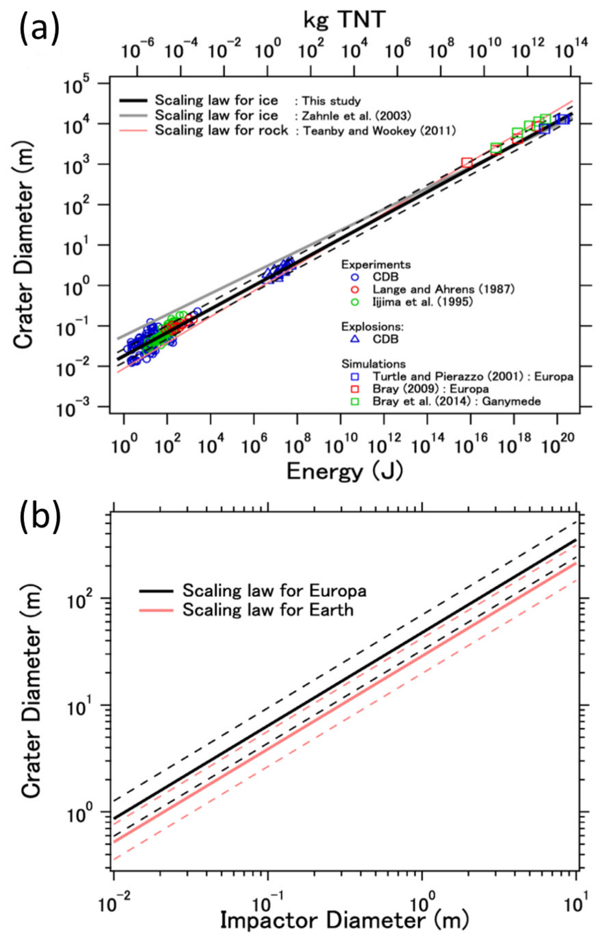

Figure 2: (a) Relation between impactor energy and crater diameter under Earth's gravity for icy surfaces. Symbols show measurements and simulations of ice impacts and explosions. Lines show scaling relations for ice (Zahnle et al., 2003, and this study) and rocky surfaces (Teanby and Wookey, 2011) for comparison. (b) Scaling relation between impactor diameter and crater diameter derived from Eq. (2) under Earth and Europa gravity conditions for an impact velocity of 26 $\mathrm{km\,s^{-1}}$ and an impactor density of 600 $\mathrm{kg\,m^{-3}}$ (Zahnle et al., 2003).

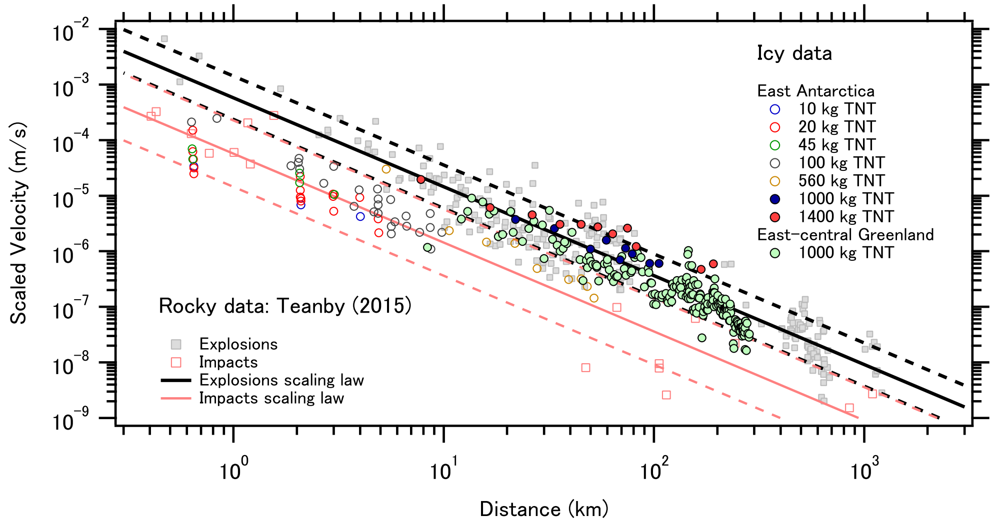

Figure 3: Relationship between the source-receiver distance and P-wave amplitudes scaled to those of a 1000 kg TNT explosion for icy conditions. Compiled data are explosive experiments on East Antarctica (Ito and Ikami, 1984) and East-central Greenland (Shulgin and Thybo, 2015). Explosive and impact data for rocky conditions compiled by Teanby (2015) are also shown for comparison. Note that for the data of Ito and Ikami (1984) half the peak-to-peak amplitudes are regarded as peak signal amplitudes, and for the data of Shulgin and Thybo (2015) the maximum amplitudes of refracted waves are reported as these cover our primary range of interest (>10 km distant). The scaling law of Teanby (2015), which was based on rocky data, also fits the ice sheet data well, so is used in this study.

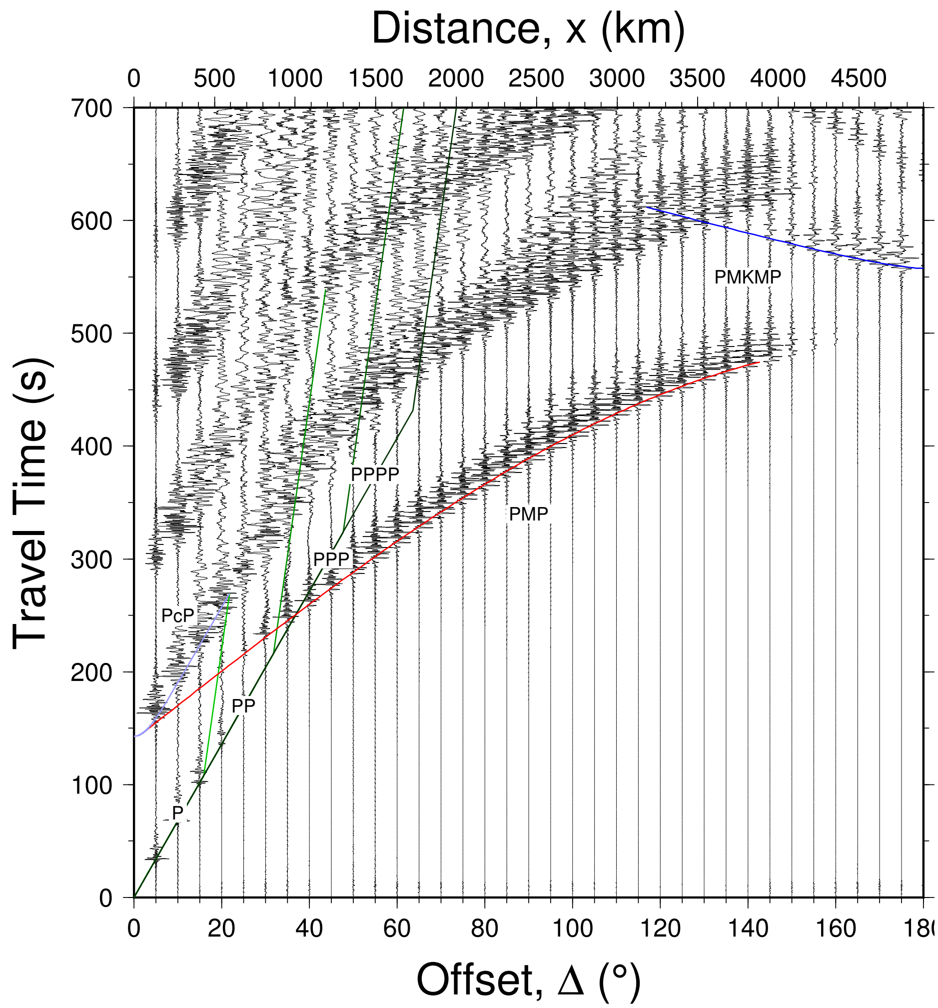

Figure 4: Record section of synthetic seismograms for an impact on Europa. The first arrival phase is the direct P-wave for offsets $\Delta < 35°$ and the mantle-refracted phase (here referred to as PMP) for $\Delta > 35°$. Late arriving low frequency reverberations are the mantle reflections (e.g. PcP) and multiples. Here "M" refers to propagation through the mantle, "c" is a reflection from the mantle, and "K" is propagation through the core. For numerical reasons the maximum frequency modelled was 0.5 Hz so the relative amplitudes are only approximate; amplitudes will be underestimated for high frequency body wave P and PMP phases. Therefore, this record section is used purely as a guide to aid the ray tracing calculations; it shows that P and PMP are are the main phases that must be considered.

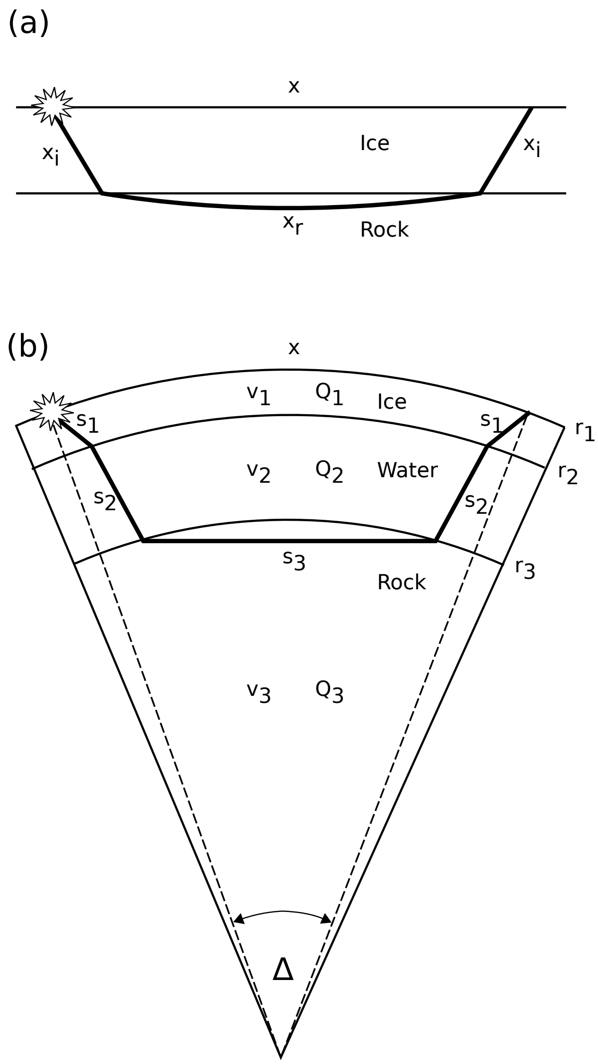

Figure 5: Ray geometry for (a) terrestrial ice sheet analogue explosion experiments and (b) Europa impacts. (a) For the terrestrial ice sheet experiments the path length though ice x_i is small compared to the path length through rock x_r, so $x_r \approx x$. (b) For Europa the curvature must be considered and requires calculation of the path lengths $s_{1,2,3}$ in each layer using simple spherical ray theory. Each layer has P-wave velocity $v_{1,2,3}$, seismic quality factor $Q_{1,2,3}$, and layer-top to planet-centre radial distance $r_{1,2,3}$. Using spherical ray theory the distance travelled through each layer can be tabulated as a function of x or Δ, where $x = r_1\Delta$.

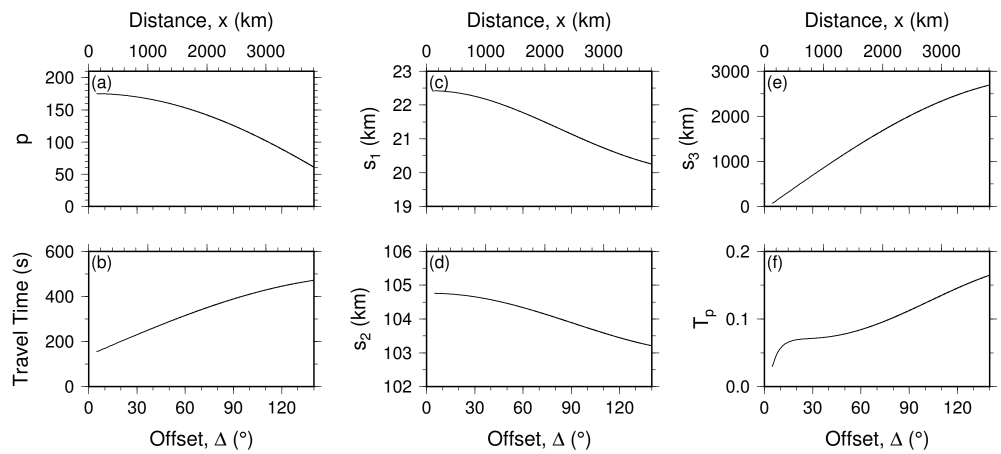

Figure 6: Ray tracing results as a function of source-receiver offset for the mantle-refracted PMP-wave. (a) The spherical ray parameter $p = ru \sin\theta$ is conserved along each ray path, where r is the distance to the planet centre, u is the slowness (inverse velocity), and θ is the angle of inclination to the local vertical. A ray parameter of p=0 represents an incidence angle of 0° (vertical propagation). (b) Travel time of the PMP-wave. (c,d,e) Path lengths through the ice crust (s_1), water ocean (s_2), and rocky mantle (s_3). (f) Combined transmission coefficient for the PMP-wave, including the effects of the ice-water, water-rock, rock-water, and water-ice interfaces encountered along the ray path. Transmission efficiency increases for decreasing incidence angle as less energy is reflected or converted into S-waves. Note that Δ=140–180° is not modelled as this is the core shadow zone.

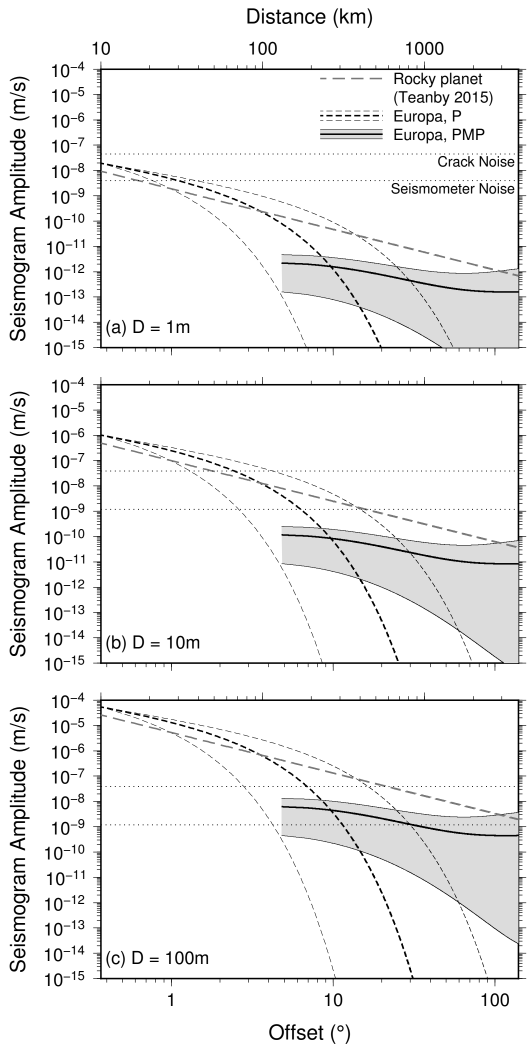

Figure 7: Maximum seismogram amplitude for P and PMP-waves as a function of distance for 1, 10, and 100 m diameter cratering events. High-, nominal-, and low-Q interior models are shown with the upper, middle, and lower curves for each arrival. P amplitude is calculated using Eq. 23 and PMP amplitude is calculated using Eqs. 24–27 with a nominal frequency of 2 Hz. The scaling law for the crustal/upper mantle-refracted P-wave in a rocky planet from Teanby (2015) is shown for comparison. Direct P-waves dominate for offsets less than 10°, beyond which PMP is the most energetic. Direct P-wave amplitude reduces rapidly with distance due to the large attenuation of ice compared to rock. The largest contributor to amplitude uncertainty is uncertainties in Q. Amplitudes have an additional factor of five uncertainty (not shown) due to conversion from crater diameter to amplitude (see Table 1). Horizontal dotted lines indicate different noise level assumptions. An arrival is considered detectable if it has an amplitude above the noise.

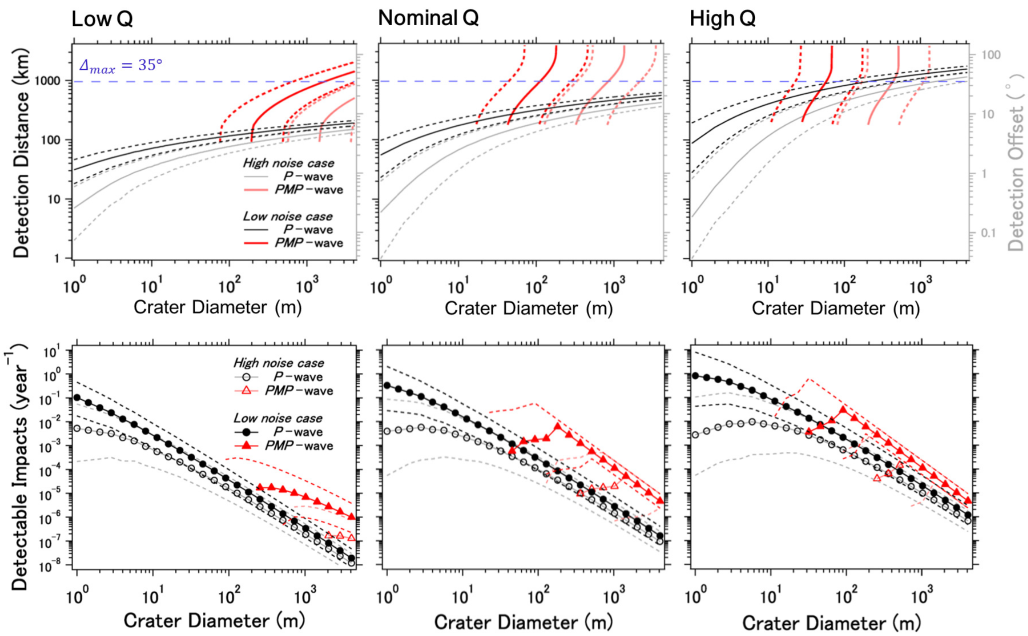

Figure 8: Seismic detectability of meteorite impacts on Europa. Upper panels show the maximum source-receiver distance/offset for a detection above the noise as a function of crater diameter for P and PMP phases. The light blue dotted line labelled Δ_{max} indicates an offset of 35°, where PMP takes over from P as the first arriving phase. However, due to the strongly attenuating ice crust the amplitude of the direct P-waves is smaller than the refracted waves for offsets $\gtrsim 10°$, so at moderate to large offsets PMP becomes the more detectable phase. Lower panels show the number of detectable impacts per year based on the impact rate model of Levison et al. (2000). Crater diameter bins are in $\sqrt{2}$ intervals following Hartmann (2005). Results are shown for three Q attenuation models: (left) Low-Q, (centre) Nominal-Q, and (right) High-Q models. Dashed curves represent 1σ uncertainties.